

# InMAP: a new model for air pollution interventions

C. W. Tessum, J. D. Hill, and J. D. Marshall

March 21, 2016

## Abstract

Mechanistic air pollution models are essential tools in air quality management. Widespread use of such models is hindered in part by the extensive expertise or computational resources needed to run most models. Here, we present InMAP (Intervention Model for Air Pollution), which offers an alternative to comprehensive air quality models for estimating the air pollution health impacts of emission reductions and other potential interventions. InMAP estimates annual-average changes in primary and secondary fine particle ( $PM_{2.5}$ ) concentrations – the air pollution outcome generally causing the largest monetized health damages – attributable to annual changes in precursor emissions. InMAP leverages pre-processed physical and chemical information from the output of a state-of-the-science chemical transport model (WRF-Chem) within an Eulerian modeling framework, to perform simulations that are several orders of magnitude less computationally intensive than comprehensive model simulations. InMAP uses a variable resolution grid that focuses on human exposures by employing higher spatial resolution in urban areas and lower spatial resolution in rural and remote locations and in the upper atmosphere; and by directly calculating steady-state, annual average concentrations. In comparisons run here, InMAP recreates WRF-Chem predictions of changes in total  $PM_{2.5}$  concentrations when run with the same spatial grid with population-weighted mean fractional error (MFE) of 17% and bias (MFB) of -11% and population-weighted  $R^2 \geq 0.92$ . Potential uses of InMAP include studying exposure, health, and environmental justice impacts of potential shifts in emissions for annual-average  $PM_{2.5}$ . The InMAP model source code and input data are freely available online.

## 1 introduction

Ambient air pollution is estimated to kill over three million people per year globally (Lim et al., 2012; Lelieveld et al., 2015). Reducing air pollution and its impacts is therefore a common policy goal. However, it is often unclear *a priori* which potential emission reductions would be most effective in improving air pollution and health because the chemical and physical relationships between emissions of  $PM_{2.5}$  and its precursors and the ambient concentrations that result are complex and nonlinear (Seinfeld and Pandis, 2006). To assist in decision-making, air pollution models are often used to estimate the health effects of a range of hypothetical changes in emissions.

Eulerian Chemical Transportation Models (CTMs; examples: CAMx, ENVIRON, 2011; CMAQ, Byun and Ching, 1999; WRF-Chem, Grell et al., 2005; GATOR-GCMOM, Jacobson, 2001) are powerful tools that can simulate the effectiveness of emission reductions at reducing air quality-related health impacts. Running CTM simulations generally requires dedicated experts or teams, and often is computationally expensive and time consuming. For example, a single simulation for annual exposure in the contiguous US with a 12 km spatial resolution can take multiple days to run on a high performance computing system (i.e., a “super-computer”) (Tessum et al., 2015).

The computational intensity and high degree of difficulty inherent in performing CTM simulations is a bottleneck for the rate at which air quality strategies can be evaluated, for the number of people who can perform such evaluations, and also therefore potentially the rate at which policies for improving air quality can be investigated, evaluated, potentially enacted. Therefore, there is a need for air quality models that are simpler to use; provide results more quickly than CTMs, while minimizing losses in predictive accuracy; and potentially can be run by outside experts. Here, we describe such a model.

The design of our new model reflects current understandings of the health impacts of air pollution:

1. Of the three million global deaths per year attributed to ambient air pollution, approximately 95 % are caused by fine particulate matter ( $PM_{2.5}$ ) (Lim et al., 2012; Lelieveld et al., 2015). The strongest predictor for these deaths is chronic  $PM_{2.5}$  exposure over periods of a year or more (Künzli et al., 2001; Pope III and Dockery, 2006; Brook et al., 2010). Therefore, a prediction of chronic exposure to  $PM_{2.5}$  is a good indicator of overall health impacts from air pollution.
2.  $PM_{2.5}$  can travel long (e.g., intercontinental) distances but can also be highly spatially variable near emissions sources. Additionally,  $PM_{2.5}$  can be both directly emitted (“primary”) and formed in the atmosphere (“secondary”). Models that predict  $PM_{2.5}$  exposure should consider all of these aspects.
3. Air pollution-mediated health damages can be a major driver of overall environmental externalities (Delucchi, 2000; Cohon et al., 2009). Therefore, air pollution models that can be used by non-air-pollution-experts can be beneficial.

Numerous air quality models already exist that have lower operational difficulty than CTMs. As discussed in Appendix A, while each model type is well-suited to certain use-cases, none are ideal for the specific use-case we are interested in: a model for accurate and spatially detailed estimates of the human health impacts of changes in air pollutant emissions that can be used by non-specialists.

Here we develop and apply a new approach, which we implement as the Intervention Model for Air Pollution (InMAP). InMAP is designed to provide estimates of air pollution health impacts resulting from marginal changes in pollutant emissions, such as those resulting from new regulations. InMAP combines spatially-resolved annual-average physical and chemical information derived from a state-of-the-science CTM (WRF-Chem) with simplifying assumptions regarding atmospheric chemistry for cases of marginal changes in emissions. InMAP is developed here to predict changes in annual average exposure to  $PM_{2.5}$ ; as mentioned above, that outcome is estimated to cause 95 % of air quality-related mortalities. Features of InMAP include reductions in computational cost relative to CTMs, yet with more spatially detailed results than are available with existing reduced-complexity models, a variable-resolution grid that focuses on human exposures by employing higher spatial resolution in urban areas and lower spatial resolution in rural and remote locations and at high altitude; and the ability to account for spatially variable aspects of secondary  $PM_{2.5}$  formation while also being amenable to running many scenarios and theoretically simple enough for use by non-experts. InMAP is designed to be informed by the default output of a single CTM run, so CTM runs that were originally created for other purposes can be used to create InMAP inputs. Limitations of InMAP include reduced accuracy as compared to CTM models and possibly increased computational expense as compared to Gaussian plume models. To our knowledge, the modeling approach developed here is the first of its kind for air pollution. It was inspired by recent advancements in reduced complexity sediment transport modeling (Liang, 2013; Liang et al., 2015).

## 2 Methods

### 2.1 Model formulation

The fate and transport of pollution in the atmosphere can be represented by a reaction-advection-diffusion equation:

$$\frac{\partial C_i}{\partial t} = \nabla \cdot (D \nabla C_i) - \nabla \cdot (\vec{v} C_i) + \sum_{j=1}^n R_{i,j} + E_i - d_i \quad (1)$$

where  $C_i$  is the concentration of one of  $n$  model pollutant species,  $D$  is a molecular diffusion coefficient (neglected here as a negligible source of chemical transport in the atmosphere compared to advection),  $\vec{v}$  is the wind vector,  $\sum_{j=1}^n R_{i,j}$  is the net formation rate of species  $i$  from species  $j$ ,  $E_i$  is pollutant emission, and  $d_i$  is pollutant removal via wet and dry deposition. InMAP estimates pollutant concentrations by estimating

a steady-state solution to Eq. (1), yielding annual average pollutant concentration results. To do so, we replace each of the terms on the right-hand side of Eq. (1) with parameterizations suitable for numerical solution as described below.

InMAP solves Eq. (1) for model chemical species comprised of primary PM<sub>2.5</sub>, volatile organic compounds (VOCs), secondary organic aerosol (SOA), sulfur dioxide (SO<sub>x</sub>), particulate sulfate (*p*SO<sub>4</sub>), oxides of nitrogen (NO<sub>x</sub>), particulate nitrate (*p*NO<sub>3</sub>), ammonia (NH<sub>3</sub>), and particulate ammonium (*p*NH<sub>4</sub>). InMAP assumes that primary PM<sub>2.5</sub>, VOCs, SOA, and SO<sub>x</sub>, NO<sub>x</sub>, and NH<sub>3</sub> can be emitted directly; the other species are secondary products formed in the atmosphere. InMAP assumes atmospheric particle diameter and density—which it only uses to calculate dry deposition rate—to be constant at 0.3  $\mu\text{m}$  and 1830 kg m<sup>-3</sup>, respectively.

### 2.1.1 Spatial discretization

Air pollution model simulations with increased spatial resolution can potentially provide improved exposure predictions (Fountoukis et al., 2013), and often yield higher overall health impact estimates (Tessum et al., 2014; Li et al., 2015). CTMs typically employ a regular (i.e., fixed-resolution) horizontal grid; to increase spatial resolution over important areas they may use a small number of higher-resolution “nested” grids inside a lower resolution outer grid. InMAP instead employs a variable resolution rectangular grid where grid cell size varies throughout the domain. To optimally focus computational resources on understanding exposures and health impacts, grid cells are smaller in urban areas and larger in rural and remote areas. Horizontal resolution also varies with height: because horizontal variability in concentrations decreases with height above the ground, we employ a low-resolution horizontal grid for all cells above a specific height (here, set to approximately 1500 m). As shown in Fig. 1, we use here a spatial domain which covers the contiguous US, southern Canada, and northern Mexico, with grid cell edge lengths ranging between 1 and 48 km. The algorithm used to determine grid cell resolution is designed to be easily adaptable to different grid cells sizes and populations and is described in detail in Appendix C.

### 2.1.2 Temporal discretization

Instead of solving for pollutant concentrations at specific points in time using temporally explicit input data as CTMs do, InMAP directly estimates annual average pollutant concentrations using annual average input data and numerical integration. We selected this approach because, as mentioned above, the vast majority of monetized damages from air pollution are attributable to human mortality from chronic (annual or longer) exposure to PM<sub>2.5</sub>.

To reach a steady-state solution, InMAP starts with an initial guess of the changes in concentrations caused by an emissions scenario (the initial guess is that there are no changes in concentrations) and iterates the model forward in time until the concentrations converge to a steady-state solution (i.e., until the predicted concentrations no longer change as the model continues to run). The integration time step  $\Delta t$  is chosen using the Courant–Friedrichs–Lowy condition (Courant et al., 1928) as in Eq. (2):

$$\Delta t = \frac{C_{\max}}{\sqrt{3}} \left( \max \left[ \frac{|U_i| + |\tilde{U}_i|}{\Delta x_i}, \frac{|V_i| + |\tilde{V}_i|}{\Delta y_i}, \frac{|W_i|}{\Delta z_i} \right]; i = 1 \dots n \right)^{-1} \quad (2)$$

where  $C_{\max}$  is the maximum allowable Courant number (set to 1.0 for InMAP), the  $U$ ,  $V$ , and  $W$  variables are annual average wind speeds in each grid cell  $i$  of  $n$  total grid cells as defined below,  $|\tilde{U}_i|$  and  $|\tilde{V}_i|$  are annual average absolute wind speed deviations as described below, and  $\Delta x$ ,  $\Delta y$ , and  $\Delta z$  are the dimensions of each grid cell. With the model settings described here  $\Delta t \sim 1$  min, and is limited by the Courant number in the 1 km grid cells near ground level (typical annual average ground-level wind speed: 1 to 8 m s<sup>-1</sup>). At the top of the model domain where wind speeds are relatively fast (up to 30 m s<sup>-1</sup> annual average), InMAP uses relatively large (48 km) grid cells to allow larger time steps. In contrast, in CTMs with constant-resolution grids,  $\Delta t$  is often limited by conditions in the top grid cells rather than at ground-level, so a 1 min time step typically corresponds to a horizontal resolution grid of 10 km. The net result is a similar  $\Delta t$  in InMAP as in a typical CTM ( $\sim 1$  min), but with smaller ground-level grid cells in InMAP relative to in a typical CTM.

During each time step in each grid cell, InMAP first adds the flux of new emissions, accounting for plume rise from elevated sources (American Society of Mechanical Engineers (ASME), 1973) (as cited in Seinfeld and Pandis, 2006). The model then calculates how changes in pollutant concentrations are affected by physical and chemical processes including advection, turbulent mixing, atmospheric aerosol chemistry, dry deposition, and wet deposition. Each process, with the exception of the instantaneous gas- vs. particle-phase partitioning of organic, nitrate, and ammonia compounds, uses an algorithm that calculates changes in concentrations based on the concentration at the beginning of the time step rather than the concentration output by other process algorithms during the same time step. Therefore, the concentrations resulting from these steps do not depend on the order of process integration. The instantaneous gas-particle partitioning, the result of which is theoretically influenced by the order of integration, is performed last.

### 2.1.3 Input data

To reduce model complexity and runtime in the InMAP model itself, an InMAP preprocessor uses the output of a more comprehensive model – here, the WRF-Chem model as configured and run by Tessum et al. (2015) – to extract emergent atmospheric properties.

Many of the chemical and physical processes important to the fate and transport of air pollution vary with the time of day and the season. A steady-state, annual-average model risks being unable to represent the results of these temporally-explicit phenomena. InMAP mitigates this potential limitation by using temporally explicit information wherever possible when calculating annual average input properties. For instance, the gas-phase oxidation of  $\text{SO}_2$  to  $\text{SO}_4^{2-}$  is represented as the product of the  $\text{SO}_2$  concentration and a reaction rate constant, but the reaction rate constant has a non-linear dependence on temperature and on the concentration of hydroxyl radical ( $\text{HO}^*$ ), both of which are temporally variable. To represent the formation of particulate  $\text{SO}_4$  ( $p\text{SO}_4$ ), InMAP needs an annual average rate constant. To capture some of the effects of temporal variability, instead of calculating the rate constant using annual average values for temperature and  $\text{HO}^*$ , we instead use temporally explicit temperatures, solar radiation intensities, and  $\text{HO}^*$  concentrations to then calculate rate constants for every hour during the year, and then take the average of these 8760 rate-constant values. Thus, the reaction rate InMAP uses for a given grid cell is an annual-average rate, not a rate calculated using annual-average values for input parameters.

In addition to  $\text{SO}_2$  oxidation rates, information collected or inferred from the comprehensive model includes spatially explicit annual averages of wind vectors, eddy diffusivity and convective transport coefficients (annual average coefficients calculated using temporally explicit wind speed, temperature, pressure, friction velocity, boundary layer height, and heat flux information), dry and wet deposition rates of various pollutants (annual average rates calculated using temporally explicit wind speed, land cover, stability, and precipitation information), gas/particle phase partitioning for pollutants (described below), and parameters relevant to the calculation of emissions plume rise (annual averages of scalar windspeed; windspeed to the powers of  $-1$ ,  $-1/3$ , and  $-1.4$ ; temperature; and two parameters related to atmospheric stability). A full list of WRF-Chem variables used by the InMAP preprocessor is available in Appendix B.

### 2.1.4 Advection

The wind velocity that is responsible for advection ( $\nabla \cdot (\vec{v}C)$  in Eq. 1) varies at time scales smaller than can be resolved by InMAP or by comprehensive CTMs. Therefore, variables  $\vec{v}$  and  $C$  in the advective transport term of Eq. (1) are commonly split up into resolved and unresolved components using Reynolds decomposition. CTMs typically split each variable  $x$  into two parts: one representing the average quantity of the variable during a model timestep ( $\bar{x}$ ) and one representing the variable variability during the same timestep ( $x'$ ). In order for InMAP to make predictions based on annual average information, it splits each variable into three parts instead of two:  $\vec{v} = \bar{\vec{v}} + \tilde{\vec{v}} + \vec{v}'$  and  $C = \bar{C} + \tilde{C} + C'$ , where  $\bar{v}$  and  $\bar{C}$  represent annual average quantities,  $\tilde{v}$  and  $\tilde{C}$  represent deviations from the annual average that are temporally resolved by the underlying CTM (WRF-Chem in this case), and  $\vec{v}'$  and  $C'$  represent deviations that are not temporally resolved by the underlying CTM. Substituting these decomposed variables into the advection term of Eq. (1)

yields Eq. (3).

$$\nabla \cdot (\vec{v}C_i) = \nabla \cdot (\bar{v}\bar{C}_i) + \nabla \cdot (\tilde{\bar{v}}\tilde{C}_i) + \nabla \cdot (\bar{v}'\tilde{C}_i) + \nabla \cdot (\tilde{\bar{v}}C'_i) + \nabla \cdot (\bar{v}'C'_i) \quad (3)$$

InMAP discretizes  $\nabla \cdot (\bar{v}\bar{C}_i)$  using the upwind advection scheme shown in Eq. (4):

$$\frac{\Delta C_i}{\Delta t} = \begin{cases} \frac{\sum_{w_j=1}^{n_{w,i}} U_i C_{w_j} f_{w_j}}{\Delta x}, & \text{if } U_i \geq 0 \\ \frac{\sum_{w_j=1}^{n_{w,i}} U_i C_i f_{w_j}}{\Delta x}, & \text{if } U_i < 0 \end{cases} \quad (4)$$

where  $\Delta C_i$  is the change in volume-specific pollutant concentration in grid cell  $i$  caused by advection between cell  $i$  and each cell  $w_j$  of  $n_{w,i}$  adjacent cells to the West during time step  $\Delta t$ . Because grid resolution varies, each cell may have more than one adjacent cell in each direction.  $U_i$  is the annual average wind velocity vector component in the East–West direction at the interface between cells  $i$  and  $w_i$ ,  $C_i$  and  $C_{w_i}$  are concentrations in their respective grid cells at the beginning of the time step,  $f_{w_j}$  is the fraction of the edge of grid cell  $i$  that is touching neighbor  $w_j$ , and  $\Delta x_i$  is the length of the grid cell in the East–West direction. Eq. (4) is repeated for neighbors to the East, to the South, to the North, above, and below cell  $i$ .

We chose the upwind advection scheme for its computational efficiency. A limitation of this scheme is that it is numerically diffusive, but this limitation is mitigated in InMAP because the variable resolution model grid uses smaller grid cells in high-population areas and thus limits numerical diffusion in the areas where accurate predictions are most important.

InMAP parameterizes  $\nabla \cdot (\tilde{\bar{v}}\tilde{C}_i)$  using the diffusion scheme shown in Eq. (5):

$$\frac{\Delta C_i}{\Delta t} = \frac{\sum_{w_j=1}^{n_{w,i}} |\tilde{U}_i| (C_{w_j} - C_i) f_{w_j}}{\Delta x} \quad (5)$$

where  $|\tilde{U}_i|$  is the annual average absolute deviation of wind speed in the East–West direction, as calculated by WRF-Chem, at the interface between cells  $i$  and  $w_j$ . Eq. (5) is repeated for neighbors to the East, to the South, to the North, above, and below cell  $i$ . This scheme assumes that deviations from annual average wind velocity are symmetrical about each axis.

Finally, InMAP parameterizes  $\nabla \cdot (\bar{v}'C'_i)$  using the combined local-nonlocal mixing scheme described in Section 2.1.5. We assume that the remaining two terms in Eq. (3),  $\nabla \cdot (\bar{v}'\tilde{C}_i)$  and  $\nabla \cdot (\tilde{\bar{v}}C'_i)$ , account for a relatively small fraction of chemical transport; finding suitable parameterizations for these two terms is an area for future research.

As shown above, to represent temporally-variable advection in an annual average modelling framework, InMAP splits advective transport into three steps, one of which is advective in nature and two of which are diffusive in nature. One result of this is that in some cases information regarding transport direction may be lost. For instance, an extreme case were wind travels from the Northwest half of the time at  $2 \text{ ms}^{-1}$  and from the Southeast the other half of the time at  $2 \text{ ms}^{-1}$  would be represented by InMAP as advection at  $0 \text{ ms}^{-1}$  and diffusive mixing equally in all directions at  $\sqrt{2} \text{ ms}^{-1}$ .

For advection and mixing, InMAP assumes zero concentration-change boundary conditions at the lateral and top edges of the model domain and an impermeable boundary at the bottom edge of the domain.

### 2.1.5 Mixing

For mixing (i.e., pollutant transport that is not resolved by WRF-Chem;  $\nabla \cdot (\bar{v}'C'_i)$  in Eq. 3) within the planetary boundary layer, we use a combined local-nonlocal closure scheme (Pleim, 2007). For mixing above the boundary layer and for horizontal mixing, we only consider turbulent mixing (Wilson, 2004). We modify Pleim's (Pleim, 2007) Eq. (10) as shown in our Eq. (6) to allow a variable number of adjacent cells and to

include horizontal and vertical mixing.

$$m_{g,i} = \sum_{g_j}^{1,n_{g,i}} (\text{M2u}_i C_{g_j} f_{g_j}) \quad (6)$$

$$m_{a,i} = \sum_{a_j}^{1,n_{a,i}} \left( \left[ \text{M2d}_{a_j} C_{a_j} \frac{\Delta z_{a_j}}{\Delta z_i} - \text{M2d}_i C_i + \Delta z_i^{-1} K_{zz,a_j} \frac{2(C_{a_j} - C_i)}{\Delta z_i + \Delta z_{a_j}} \right] f_{a_j} \right) \quad (7)$$

$$m_{b,i} = \sum_{b_j}^{1,n_{b,i}} \left( \Delta z_i^{-1} K_{zz,b_j} \frac{2(C_{b_j} - C_i)}{\Delta z_i + \Delta z_{b_j}} f_{b_j} \right) \quad (8)$$

$$m_{w,i} = \sum_{w_j}^{1,n_{w,i}} \left( \Delta x_i^{-1} K_{xx,w_j} \frac{2(C_{w_j} - C_i)}{\Delta x_i + \Delta z_{w_j}} f_{w_j} \right) \quad (9)$$

$$m_{e,i} = \sum_{e_j}^{1,n_{e,i}} \left( \Delta x_i^{-1} K_{xx,e_j} \frac{2(C_{e_j} - C_i)}{\Delta x_i + \Delta x_{e_j}} f_{e_j} \right) \quad (10)$$

$$m_{s,i} = \sum_{s_j}^{1,n_{s,i}} \left( \Delta y_i^{-1} K_{yy,n_j} \frac{2(C_{s_j} - C_i)}{\Delta y_i + \Delta y_{s_j}} f_{s_j} \right) \quad (11)$$

$$m_{n,i} = \sum_{n_j}^{1,n_{n,i}} \left( \Delta y_i^{-1} K_{yy,n_j} \frac{2(C_{n_j} - C_i)}{\Delta y_i + \Delta y_{n_j}} f_{n_j} \right) \quad (12)$$

$$\Delta C_i = (m_{g,i} + m_{a,i} + m_{b,i} + m_{w,i} + m_{e,i} + m_{s,i} + m_{n,i}) \Delta t \quad (13)$$

In Eqs. (6–13),  $C_i$  refers to the pollutant concentration in grid cell  $i$ ,  $g_j$  refers to one of  $n_{g,i}$  cells at ground level directly below the cell of interest, and  $b_j$ ,  $a_j$ ,  $w_j$ ,  $e_j$ ,  $s_j$ , and  $n_j$  refer to cells directly below, above, west, east, south, and north of the cell of interest. M2u and M2d are upward and downward convective mixing coefficients (Pleim, 2007).  $K_{zz}$  is the turbulent mixing coefficient in the vertical direction, and  $K_{xx}$  and  $K_{yy}$  are horizontal mixing coefficients. We calculate mixing coefficients (both local and nonlocal) for each time step in the WRF-Chem model output, using the boundary layer height specific to that time step, and then use the average of these values to represent mixing in InMAP.

### 2.1.6 Chemistry

In InMAP, total PM<sub>2.5</sub> is comprised of primary PM<sub>2.5</sub>, which is assumed to be nonvolatile and nonreactive, and secondary PM<sub>2.5</sub> which can be formed from VOCs, SO<sub>x</sub>, NO<sub>x</sub>, or NH<sub>3</sub>. To model the secondary formation of PM<sub>2.5</sub> ( $R$  in Eq. 1), InMAP estimates formation of particulate sulfate and ammonium using first-order chemical reaction kinetics. Partitioning between the gas and aerosol phases for nitrogen oxide, ammonia, and organic compounds (VOCs and SOA) is done assuming instantaneous adjustment to match equilibrium partitioning coefficients. Because InMAP is designed to predict the impacts of marginal changes in emissions and because the chemical relationships are nonlinear, we calculate reaction rates and partitioning coefficients for marginal changes in concentrations.

There are two main pathways from sulfur dioxide (SO<sub>2</sub>) gas to sulfate (SO<sub>4</sub><sup>2-</sup>) particles: gas phase oxidation by hydroxyl radical (HO\*) and aqueous phase oxidation by hydrogen peroxide (H<sub>2</sub>O<sub>2</sub>) (Seinfeld and Pandis, 2006). There are no major pathways for reaction of SO<sub>4</sub><sup>2-</sup> back to SO<sub>2</sub>. After calculating an annual average overall reaction rate  $k_S$  for SO<sub>2</sub> to SO<sub>4</sub><sup>2-</sup> using WRF-Chem output data and formulas for the gas phase and aqueous pathways from Seinfeld and Pandis (2006), we calculate the formation of SO<sub>4</sub><sup>2-</sup> particles from SO<sub>2</sub> gas as in Eq. (14):

$$\Delta C_{S,g2p,i} = k_{S,i} C_{S,g,i} \Delta t \quad (14)$$

where  $\Delta C_{S,g2p,i}$  is the transformation of sulfur from gas to particle phase during time step  $\Delta t$  in cell  $i$  and  $C_{S,g,i}$  is the gas phase concentration of sulfur at the beginning of the time step.

For  $\text{NO}_x$ ,  $\text{NH}_3$ , and VOCs, the chemical reaction mechanisms governing partitioning between the gas and particle phase are more complex than the reactions driving sulfate formation. They are also reversible: gas-phase compounds can convert to aerosols and then back to gas-phase, and the direction of the reactions can vary according to the time of day and according to the season. It is not possible to directly represent these reactions in a steady-state, annual average model such as InMAP. For  $\text{NO}_x$ ,  $\text{NH}_3$ , and VOCs we instead calculate an annual average partitioning coefficient  $f_{p,i}$  in grid cell  $i$  for marginal changes in concentrations from the WRF-Chem output data as in Eq. (15):

$$f_{p,i} = \sum_{j=1}^n \left( \frac{\Delta m_{p,i,j}}{\Delta m_{p,i,j} + \Delta m_{g,i,j}} \right) / n \quad (15)$$

where  $\Delta m_{p,i,j}$  is change in mass in cell  $i$  the particle phase and  $\Delta m_{g,i}$  is change in mass in the gas phase from one WRF-Chem output time step  $j$  to the next, and  $n$  is the total number of output time steps (8760). Then, we use this coefficient to calculate gas/particle partitioning in InMAP using Eqs. (16) and (17):

$$C_{p,i,f} = (C_{g,i,s} + C_{p,i,s}) f_{p,i} \quad (16)$$

$$C_{g,i,f} = (C_{g,i,s} + C_{p,i,s}) (1 - f_{p,i}) \quad (17)$$

where  $C_{g,i,s}$ ,  $C_{p,i,s}$ ,  $C_{g,i,f}$  and  $C_{p,i,f}$  are gas and particle phase concentrations in cell  $i$  at the start  $s$  and end  $f$  of the time step. The concentration at the end of one time step is used as the concentration at the beginning of the next time step. For partitioning between VOCs and secondary organic aerosol (SOA) we only consider those VOCs that are SOA precursors as defined by Ahmadov et al. (2012).

### 2.1.7 Wet and dry deposition

Following Seinfeld and Pandis (2006), we assume that dry deposition  $v_{dd,i}$  for gases in cell  $i$  can be represented as a function of resistances in series as in Eq. (18), where  $r_{a,i}$  is aerodynamic resistance,  $r_{b,i}$  is quasi-laminar boundary layer resistance, and  $r_{c,i}$  is surface resistance. For particles, this equation is slightly altered to account for settling velocity. We calculate an annual average dry deposition velocity for each ground-level grid cell using the output from WRF-Chem and algorithms for  $r_{c,i}$  for gases from Wesely (Wesely, 1989; Walmsley and Wesely, 1996). To calculate  $r_{c,i}$  for particles, and to calculate  $r_{a,i}$  and  $r_{b,i}$ , we use algorithms from Seinfeld and Pandis (2006). We then calculate dry deposition within InMAP using Eqs. (18) and (19):

$$|v_{dd,i}| = (r_{a,i} + r_{b,i} + r_{c,i})^{-1} \quad (18)$$

$$\Delta C_i = -C_i v_{dd,i} \frac{\Delta t}{\Delta z_i} \quad (19)$$

where  $C_i$  is pollutant concentration in a grid cell in the lowest model layer.

We calculate an annual average wet deposition rate  $r_{wd,i}$  for each grid cell  $i$  using output from WRF-Chem and a simple algorithm from the EMEP model (Simpson et al., 2003) that estimates a rate of wet deposition from in-cloud and below-cloud scavenging rate as a function of cloud fraction, precipitation rate, and air density. The algorithm provides separate rate estimates for particles,  $\text{SO}_2$ , and other gases. We then calculate wet deposition within InMAP using Eq. (20):

$$\Delta C_i = -C_i r_{wd,i} \Delta t \quad (20)$$

Dry deposition is only assumed to occur in ground-level grid cells. Wet deposition is calculated for every grid cell (with location-specific deposition rates).

## 2.2 User inputs

One goal for InMAP is ease of use. The only user-specified input required by running InMAP in its native layout is a shapefile or set of shapefiles (format specification: <http://www.esri.com/library/whitepapers/pdfs/shapefile.pdf>) containing locations of changes in annual total emissions of VOCs,  $\text{SO}_x$ ,  $\text{NO}_x$ ,  $\text{NH}_3$ , and primary fine particulate matter ( $\text{PM}_{2.5}$ ). Locations can be specified as polygon, line, or point entities, and can include stack attributes for elevated sources. InMAP allocates emissions from shapefiles to the corresponding model cells using area-weighting.

## 2.3 Performance evaluation

InMAP provides a computationally inexpensive alternative to a CTM for calculating impacts of marginal emission changes. Therefore, its performance should be evaluated in terms of predicting marginal changes in concentrations rather than total ambient concentrations. Although the strongest evaluation would be to compare InMAP predictions to measured pollutant concentrations, there do not exist nationwide, long-term measurements of the effects of marginal emissions changes on pollutant concentrations. Instead, we compare InMAP predictions for scenarios with changes in emissions to those from a CTM. It is common to evaluate air pollution sensitivity models against more complex models (Hakami et al., 2007; Zhang et al., 2012). Specifically, for our model-model evaluation we employ WRF-Chem to model 11 scenarios of emission changes that would result from the hypothetical adoption of alternative light-duty transportation technologies. These scenarios include emissions from transportation, electric generation, agriculture, and various industrial sources in proportions that vary among scenarios – since these activities have different spatial distributions, the emissions scenarios are spatially heterogeneous – resulting in total  $\text{PM}_{2.5}$  concentration changes on the order of 1 %. A brief description of each emissions scenario is provided in Figs. 12–23. Additional information regarding the emission scenarios and the associated WRF-Chem modeling can be found elsewhere (Tessum et al., 2012, 2014). Below, we also compare InMAP results against an existing reduced-form model: the COBRA source-receptor matrix (US EPA, 2012).

To explore how reliably InMAP can be expected to predict larger changes in concentrations, we separately evaluate InMAP performance in predicting measured year 2005 annual average  $\text{PM}_{2.5}$  concentrations reported by the US EPA (2005). As mentioned above, InMAP is designed to predict marginal changes in concentrations rather than total concentrations; comparing InMAP against observed values represents a use of the model that is beyond what that model was designed for. Nevertheless, we conduct and evaluate InMAP in that manner here (i.e., running it as though it were a conventional CTM rather than a model for marginal changes in emissions) to provide information on how widely applicable the model is, including its use in simulations of large changes in emissions.

Finally, to investigate InMAP’s ability to predict temporally variable pollutant transport in a steady-state framework, and its ability to predict higher-resolution pollutant spatial patterns based on lower-resolution meteorology fields, we perform an additional independent comparison of InMAP vs. WRF-Chem. To perform this comparison, we first use WRF-Chem to simulate annual average transport and fate of 100 short tons per year of emissions from a single ground-level point source of non-reactive  $\text{PM}_{2.5}$  in downtown Los Angeles, California. We run the WRF-Chem simulation over a  $9801 \times 9801$  km spatial domain with 9 km, 3 km, and 1 km nested grids. Each nested grid is comprised of  $33 \times 33$  horizontal grid cells and 30 vertical layers centered over downtown Los Angeles. We split up year 2005 into 8 approximately 45 day periods and simulate approximately the first 15 days of each period with WRF-Chem to approximate annual average conditions. All other aspects of WRF-Chem configuration are as described by Tessum et al. (2015). We use the results from the 9 km-resolution outer WRF-Chem domain to create two versions of InMAP: one with 9 km grid cells aligning with the native WRF-Chem grid cells (“InMAP LA-9km”), and one with 1–27 km variable resolution grid cells (“InMAP LA-variable”). The 3 km- and 1 km-resolution inner WRF-Chem domains are not used during the setup of InMAP. We then compare InMAP LA-9km against the 9 km resolution WRF-Chem results and we compare InMAP LA-variable against the 1 km resolution WRF-Chem results.

We use several metrics to assess model-model and model-measurement agreement, including mean bias (MB, Eq. 21), mean error (ME, Eq. 22), mean fractional bias (MFB, Eq. 23), mean fractional error (MFE,

Eq. 24), and model ratio (MR, Eq. 25), as well as linear regression slope ( $S$ ), intercept ( $I$ ), and squared Pearson correlation coefficient ( $R^2$ ) values. In Eqs. (21)–(25),  $i$  corresponds to one of  $n$  comparisons, and  $X$  and  $Y$  are the annual average modeled or measured values we are comparing.

$$\text{MB} = \frac{1}{n} \sum_{i=1}^n (Y_i - X_i) \quad (21)$$

$$\text{ME} = \frac{1}{n} \sum_{i=1}^n |Y_i - X_i| \quad (22)$$

$$\text{MFB} = \frac{1}{n} \sum_{i=1}^n \frac{2(Y_i - X_i)}{(Y_i + X_i)} \quad (23)$$

$$\text{MFE} = \frac{1}{n} \sum_{i=1}^n \frac{2|Y_i - X_i|}{(Y_i + X_i)} \quad (24)$$

$$\text{MR} = \frac{1}{n} \sum_{i=1}^n \frac{Y_i}{X_i} \quad (25)$$

## 3 Results

The resulting InMAP computer model is comprised of  $\sim 2000$  lines of code written in the Go language (<http://golang.org/>) with an additional  $\sim 2900$  lines of code for preprocessing WRF-Chem output data into InMAP input data. Each InMAP model run takes approximately one hour to complete on a desktop computer with an Intel Ivybridge processor. The model is freely available at <https://github.com/ctessum/inmap> (doi:10.5281/zenodo.46007) and is licensed under the GNU General Public License (GPL) v3. Results here are based on InMAP version 1.1.0.

### 3.1 Model to model comparison: full US

Figure 2 shows WRF-Chem, InMAP, and COBRA model results for one of the emissions scenarios. We show two InMAP configurations: the 12 km fixed-resolution grid that mirrors the grid used for WRF-Chem simulations (“InMAP 12 km”) and a variable-resolution grid for which the smallest cells are  $1\text{ km}^2$  (“InMAP 1 km”). Overall, spatial patterns in concentration changes are similar in InMAP, COBRA, and WRF-Chem. In the specific example shown in Fig. 2, differences in estimated concentrations are apparent in Southern California and the Gulf Coast. COBRA provides one prediction per county as can be discerned in Fig. 2d where counties are large (e.g., in Southern California around Los Angeles). Figures 12–23 contain information similar to Fig. 2 for the remaining emissions scenarios investigated here, as well as corresponding performance statistics.

Figure 3 compares InMAP, WRF-Chem, and COBRA ground-level predictions for 12 emissions scenarios. Two sets of comparisons are shown: area-weighted (useful for understanding atmospheric processes such as mixing and removal) and population-weighted (useful for human exposures and health impacts).

InMAP 12 km reproduces the WRF-Chem predictions for changes in area-weighted concentrations with  $R^2 = 0.94$  and  $\text{MFB} = -41\%$  and in population-weighted concentrations with  $R^2 = 0.92$  and  $\text{MFB} = -11\%$  (Fig. 3a). InMAP 1 km performance (Fig. 3b) is similar to that of InMAP 12 km. InMAP performance is not remarkably different from the existing COBRA model (Fig. 3c). However, InMAP has capabilities not found in COBRA, such as predicting how pollutant concentrations vary within a county or a city and accounting for spatially variable aspects of secondary PM<sub>2.5</sub> formation.

Figure 4 compares InMAP and WRF-Chem for PM<sub>2.5</sub> subgroups: primary PM<sub>2.5</sub>, particulate nitrate ( $p\text{NO}_3$ ), particulate ammonium ( $p\text{NH}_4$ ), particulate sulfate ( $p\text{SO}_4$ ), and secondary organic aerosol (SOA). InMAP primary PM<sub>2.5</sub> predictions (Fig. 4a and b) agree with WRF-Chem with  $R^2$  values of 0.97 or greater (population-weighted MFE  $\leq 21\%$ ; area-weighted MFE  $\leq 59\%$ ).

InMAP agreement with WRF-Chem results for  $p\text{NO}_3$  and  $p\text{NH}_4$  is the poorest of the species considered here ( $R^2 = 0.43\text{--}0.78$ ).  $p\text{NO}_3$  and  $p\text{NH}_4$  formation rates have large seasonal and diurnal variations, and so are more challenging to represent in a steady-state, annual average model such as InMAP.

For  $p\text{SO}_4$ , InMAP predictions are well-correlated with WRF-Chem ( $R^2 \geq 0.99$ ) but tend to underpredict concentration changes (population-weighted MFB = -50%).  $p\text{SO}_4$  formation follows comparatively simple and slow-acting chemical mechanisms as described above.

For secondary organic aerosol (SOA), InMAP predictions agree relatively well with WRF-Chem for population-weighted concentration changes (MFB = -48%,  $R^2 = 0.90$ ). InMAP underpredicts area-weighted changes in concentrations relative to WRF-Chem (MFB  $\approx -110\%$ ).

### 3.2 Model to model comparison: regional

Figure 5 shows InMAP performance by US region. (Region boundaries are in Fig. 27.) Model performance is in general similar among regions. One exception is for particulate nitrate concentrations, where InMAP reproduces WRF-Chem predictions better in the Midwest (population-weighted S = 0.78) than elsewhere (population-weighted S = 0.9–0.33). This may be explained by the presence of negative WRF-Chem predictions of  $p\text{NO}_3$  concentration changes in non-Midwest regions. These negative concentration changes are caused by interactions between  $\text{PM}_{2.5}$  subspecies that InMAP does not account for. As discussed below, these interactions are most important when changes in  $\text{NO}_x$  emissions are low, so their effect on total  $\text{PM}_{2.5}$  predictive performance is minor.

Another exception is  $p\text{SO}_4$  concentrations in the West, where InMAP underpredicts concentrations relative to WRF-Chem (population-weighted MFB = -133%). We hypothesize that, owing to relatively low population density in the West, a larger fraction of changes in  $p\text{SO}_4$  concentrations in that region may be caused by long-range transport, which is in general more difficult to accurately predict than shorter-range transport.

We additionally include grid-cell-specific comparisons between WRF-Chem and InMAP for the 12 emissions scenarios investigated here, as well as corresponding performance statistics, in Figs. 12–23. Fractional performance statistics (e.g., MFB and MFE) can be highly influenced by concentrations in the lowest-concentration cells and absolute performance statistics (e.g., MB and ME) depend in part on the magnitude of emissions in each emissions scenario. We therefore focus greatest attention on population-weighted measures. Population-weighted  $R^2$  values range between 0.01 and 0.99 among scenarios and pollutant types. The lowest  $R^2$  values reflect an atypical comparison and are not a strong indication of typical model performance, for the following reason. The lowest  $R^2$  values are observed for  $p\text{NO}_3$  and  $p\text{NH}_4$  predictions in scenarios dominated by coal power plant emissions, where nonlinear effects related to increased  $\text{SO}_2$  concentrations (which are not represented in InMAP) outweigh  $p\text{NO}_3$  and  $p\text{NH}_4$  formation from  $\text{NO}_x$  and  $\text{NH}_3$  emissions. However, these nonlinear effects are most important when changes in  $p\text{NO}_3$  and  $p\text{NH}_4$  concentrations are low, so in these cases poor performance in predicting  $p\text{NO}_3$  and  $p\text{NH}_4$  concentrations does not necessarily adversely impact InMAP performance in predicting total  $\text{PM}_{2.5}$  concentrations.

### 3.3 Model to measurement comparison

InMAP is designed to model the changes in pollutant concentrations caused by marginal changes in emissions, but there are no long-term, nationwide measurements of the impacts of changes in emissions on changes in concentrations against which to evaluate InMAP directly. Therefore, we use the model-to-model comparisons described above as our main evaluation of InMAP performance. However, we also evaluate here InMAP performance in predicting overall pollutant concentrations for the year 2005. One purpose of this comparison is as a bounding estimate of how accurate InMAP would be in predicting the impacts of large changes in emissions. Figures 6–9 show the results of this comparison in terms of overall relationships between modeled and measured values and the spatial patterns in those relationships for  $\text{PM}_{2.5}$  and its subspecies. Corresponding information for gas-phase pollutants is in Figs. 24–26. Results in Figs. 6–9 for WRF-Chem refer to the WRF-Chem model results described by Tessum et al. (2015) that we use to create InMAP inputs. In general, InMAP tends to underpredict observed total  $\text{PM}_{2.5}$  concentrations (MFB = -65%; WRF-Chem

$MFB = 14\%$ ). However, even though InMAP is designed to predict marginal changes in concentrations rather than total concentrations, it still meets published air quality model  $PM_{2.5}$  performance criteria of  $MFB \leq \pm 60\%$  and  $MFE \leq 75\%$  (Boylan and Russell, 2006) for predictions of  $pNH_4$  and  $pNO_3$ . It does not meet the performance criteria for  $pSO_4$  or for total  $PM_{2.5}$ . Figures 6–9 show that much of the InMAP underpredictions of total  $PM_{2.5}$  concentrations relative to observations are caused by underpredictions in  $pSO_4$ . This inaccuracy in predicting observed  $pSO_4$  concentrations is not unexpected because the chemical reactions that produce  $pSO_4$  are nonlinear and InMAP is designed to predict marginal  $pSO_4$  production rather than total  $pSO_4$  production. Future research could potentially re-parameterize InMAP to be a conventional (rather than marginal-change) model; that step is beyond the scope of the present article. There exist other criteria for determining model suitability (e.g., those proposed by Thunis et al. (2012)) which could be explored in future research.

### 3.4 Single source model to model comparison

Figure 10 compares WRF-Chem and InMAP concentration predictions for a single ground-level point source of primary  $PM_{2.5}$  emissions. Comparisons are included for a 9 km-resolution WRF-Chem domain (Fig. 10a) against a matching 9 km-resolution InMAP domain ("InMAP LA-9km"; Fig. 10b), and for a nested 1 km-resolution WRF-Chem domain (Fig. 10d) against a 1–27 km variable-resolution InMAP domain ("InMAP LA-variable"; Fig. 10e) that was created based on the 9 km WRF-Chem results. The main difference between the two models for the 9 km domain is that WRF-Chem predicts higher concentrations in the grid cell where the emissions are located than InMAP does. One reason for this is InMAP's use of a numerically diffusive advection scheme. The same effect can be seen in the 1 km resolution results, although these results also show that the advection solver used by WRF-Chem also creates numerical artifacts in the form of a much higher rate of transport in the exact Northward, Southward, and Westward directions from the emissions source than would generally be expected. InMAP LA-variable reproduces the spatial pattern predicted by the 1 km WRF-Chem results with  $MFB$  and  $MFE \approx 100\%$  and  $R^2 = 0.67 - 0.74$ . When interpreting these results, it is important to consider that the InMAP predictions are based on lower (9 km) resolution meteorological information from WRF-Chem and should not be expected to match the WRF-Chem predictions exactly. In most cases in Fig. 10, InMAP performance based population-weighted metrics is better than performance based on area-weighted metrics.

## 4 Discussion

We have presented here a new air quality model for determining the human health impacts of marginal changes in pollutant emissions. In comparisons run here, InMAP recreates WRF-Chem predictions of changes in total  $PM_{2.5}$  concentrations with population-weighted  $MFE$  and  $MFB < 17\%$  and  $R^2 \approx 0.92$ . Among individual  $PM_{2.5}$  species, the best predictive performance is for primary  $PM_{2.5}$  ( $MFE: 21\%$ ;  $MFB: -21\%$ ) and the worst predictive performance is for particulate nitrate ( $MFE: 145\%$ ;  $MFB: 104\%$ ). InMAP is reduced in complexity compared to comprehensive chemical transport models but more accessible to non-specialists and more spatially detailed than other reduced-complexity national-scale air quality models. One of these existing models is the COBRA model, which we show performs similarly to the InMAP model presented here in terms of reproducing WRF-Chem changes in population-weighted average concentrations. InMAP, however, has features and capabilities that make it better suited than COBRA or other existing models for certain use cases (e.g., for simulations where it is desirable to estimate within-city, or even within-county, differences in  $PM_{2.5}$  concentrations, while also estimating long range transport of  $PM_{2.5}$  in the same simulation).

Figure 11 shows a small area of the maps in Fig. 2, centered on one example urban area (Las Vegas, Nevada). COBRA represents all of the county that contains Las Vegas as having the same  $PM_{2.5}$  concentration, so most of the map is only one color. WRF-Chem, as configured here, is able to resolve differences in pollutant levels at a 12 km scale for the contiguous US (If the size of the total spatial domain were decreased to only include the area surrounding Las Vegas, WRF-Chem could resolve differences at a  $\sim 1-4$  km scale.)

InMAP is unique among existing models in that it can model changes in pollutant concentrations across the entire contiguous US with 1 km spatial resolution in all high-population areas, all in a single model run.

The ability to resolve differences in pollution concentrations within urban areas is important for certain types of analyses, such as those that seek to determine how pollution exposure differs among demographic groups (environmental justice) or neighborhoods.

InMAP is much less computationally intensive than are CTMs. For example, InMAP 1 km produces the results for each of the scenarios shown here in approximately 45 min on a current desktop computer, requiring a factor of  $\sim 25\,000$  less computational power than was required to produce the WRF-Chem results shown here. This computational speed-up makes possible uncertainty, sensitivity, and scenario analyses that could not be attempted with WRF-Chem or other comprehensive chemical transport models.

Limitations of InMAP include the following. Model performance is better for population-weighted primary PM<sub>2.5</sub>, pSO<sub>4</sub>, and SOA concentrations ( $R^2 \geq 0.85$ ) than for changes in pNO<sub>3</sub> and pNH<sub>4</sub> concentrations ( $R^2 \sim 0.4\text{--}0.8$ ). The setup and testing of InMAP has mainly considered SOA formed from anthropogenic sources; further testing is needed to determine InMAP performance in predicting impacts of biogenic VOC emissions. Additional testing could be useful to further evaluate the accuracy of InMAP's high-resolution urban area predictions against other high-resolution model simulations or measurements. At present, InMAP does not predict concentrations of ground-level ozone (O<sub>3</sub>), which is considered the distant-second largest source of human health burden from air pollution after PM<sub>2.5</sub> (Lim et al., 2012; Lelieveld et al., 2015). Additionally, InMAP performance is better for population-weighted metrics (e.g., for health studies, exposure, or environmental justice) than for area-weighted metrics (e.g., for understanding "average atmospheric" processes).

A future version of InMAP, including more comprehensive mechanisms for gas- and aerosol-phase chemistry and iterating through diurnal cycles representative of each season of the year instead of using annual average information, could potentially ameliorate many of these limitations. This approach would by necessity be more computationally intensive than the current version and require more user input information, so increased predictive power may come at the expense of ease, speed, and flexibility.

InMAP is designed to be readily adapted to different spatial and temporal domains. The main requirement to do so is output from a CTM for the desired domain. (An evaluation of model accuracy in the new domain would also be recommended.) By producing an air quality model that is computationally inexpensive to operate, relatively easily adaptable to new geographical regions, able to be operated with a moderate level of specialist knowledge, we hope to make air quality modeling more widespread, easier, and more accessible to scientists, policymakers, and concerned citizens worldwide.

## 5 Acknowledgements

The authors thank Andrew Goodkind, Dylan Millet, Dev Millstein, Arvind Singh, and Vaughan Voller for feedback and input into model development, and John Michalakes for assistance with WRF-Chem performance tuning. We also acknowledge the University of Minnesota Institute on the Environment Initiative for Renewable Energy and the Environment Grants No. RI-0026-09 and RO-0002-11, the US Department of Energy Award No. DE-EE0004397, and the US Department of Agriculture NIFA/AFRI Grant No. 2011-68005-30411 for funding; and the Minnesota Supercomputing Institute and the Department of Energy National Center for Computational Sciences Award No. DD-ATM007 for computational resources.

## A Existing reduced-complexity air quality models

### A.1 CTM-based sensitivity models

Several CTM-based tools can reduce the computational requirements of determining how changes in emissions would impact air pollution concentrations. The direct decoupled method (DDM, Zhang et al., 2012), can, for example, calculate spatially explicit changes in health impacts attributable to changes in overall emissions. The adjoint method (Hakami et al., 2007; Dedoussi and Barrett, 2014), can, for example, calculate

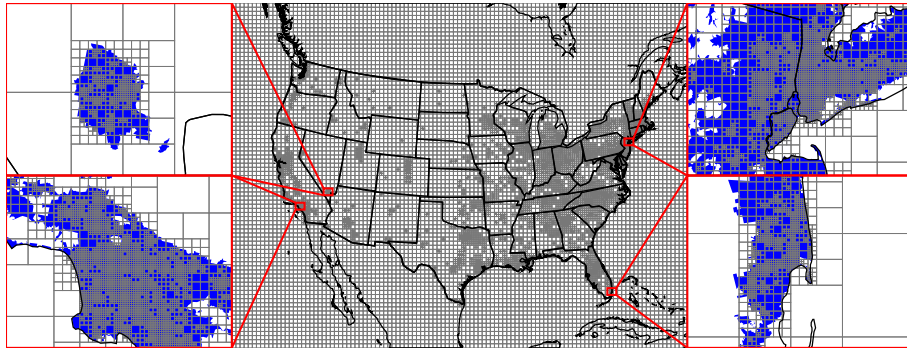


Figure 1: Spatial discretization of the model domain into variable resolution grid cells. The insets show the areas around the cities of Las Vegas, Los Angeles, New York, and Miami in detail. Blue shading represents urban areas as defined by the US Census.

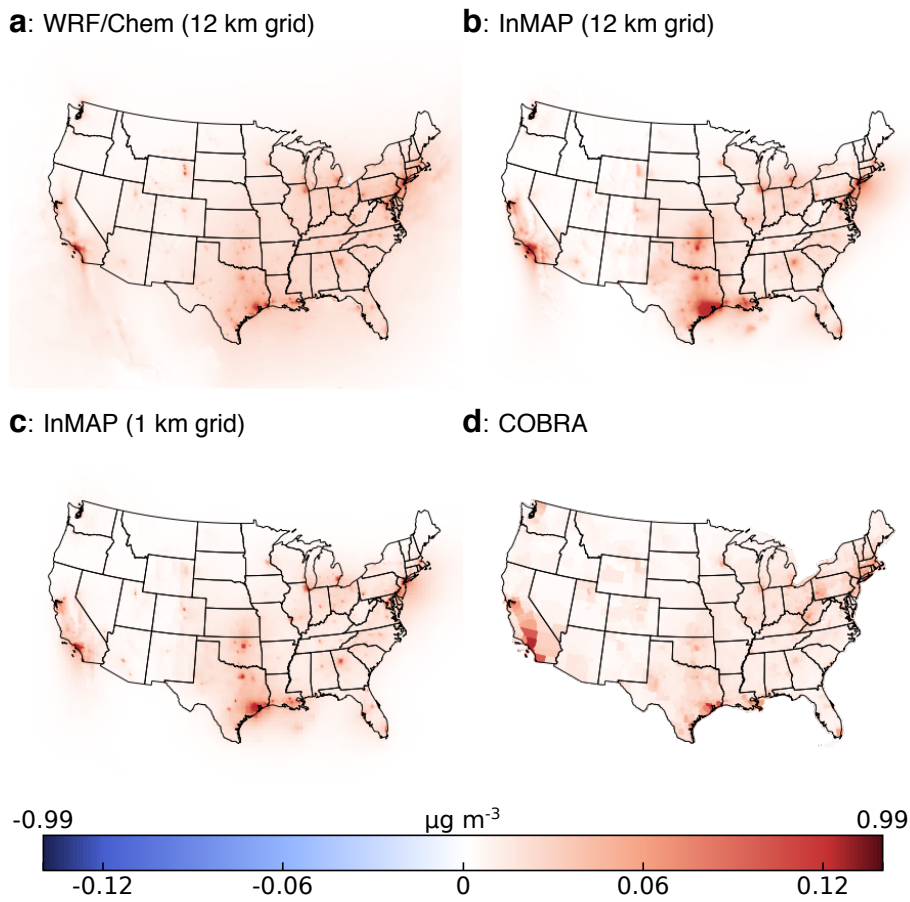


Figure 2: Changes in concentrations resulting from one emissions scenario as calculated by (a) WRF-Chem, (b) InMAP with a 12 km resolution grid, (c) InMAP with a 1 to 48 km variable resolution grid (i.e., a typical setup for InMAP), and (d) COBRA. For ease of viewing, there is a discontinuity at the 99th percentile of concentration values. Figures 12–23 provide similar information for the rest of the scenarios.

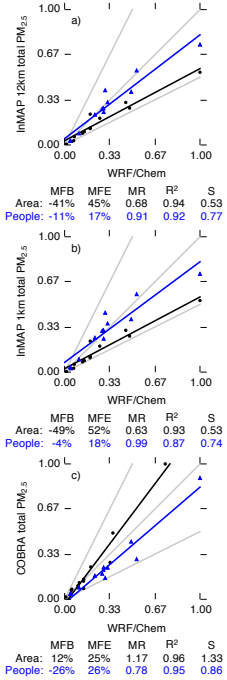


Figure 3: Comparison of total (primary plus secondary) area-weighted (black dots) and population-weighted (blue triangles) annual average predicted PM<sub>2.5</sub> concentration for WRF-Chem ( $x$  axis) and either InMAP or COBRA ( $y$  axis) for 11 emissions scenarios. To assist in comparison between area- and population-weighted predictions, concentrations shown here are normalized so that the largest value in each comparison equals one. The gray lines represent 1 : 1, 2 : 1, and 1 : 2 ratios between the models, and the black and blue lines represent least-squares regressions. Performance statistics for each comparison are listed below the plots. Abbreviations: MFB = mean fractional bias; MFE = mean fractional error; MR = model ratio;  $R^2$  = squared Pearson correlation coefficient;  $S$  = slope of regression line.

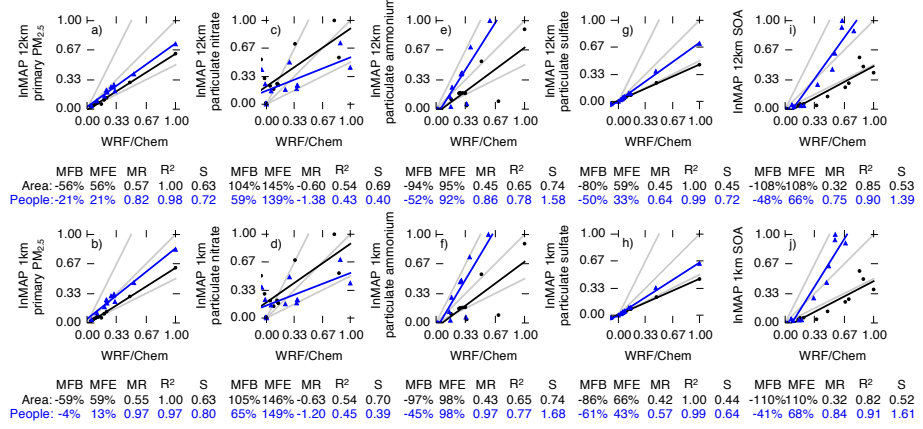


Figure 4: Comparison of area-weighted (black dots) and population-weighted (blue triangles) annual average predictions of PM<sub>2.5</sub> subspecies between WRF-Chem (*x* axis) and InMAP (*y* axis) for 11 emissions scenarios. To assist in comparison between area- and population-weighted predictions, concentrations shown here are normalized so that the largest value in each comparison equals one. The gray lines represent InMAP : WRF-Chem ratios of 1 : 1, 2 : 1, and 1 : 2. The black and blue lines represent least-squares regressions. Performance statistics for each comparison are listed below the plots. Abbreviations: MFB = mean fractional bias; MFE = mean fractional error; MR = model ratio; R<sup>2</sup> = squared Pearson correlation coefficient; S = slope of regression line.

how spatially explicit changes in emissions cause changes in overall health impacts. Source apportionment attributes pollutant concentrations or concentration sensitivities among different sources. One example of a source apportionment tool is the Particle Source Apportionment Tool (PSAT) (Wagstrom et al., 2008). All three of these approaches can be computationally inexpensive to use once the original sensitivities are calculated and are likely more accurate than the approach we present here. However, the calculated sensitivities are often not widely adaptable to different use-cases. For instance, changing the spatial distribution of emissions in the case of DDM, the spatial distribution of the human population in the case of the adjoint method, or the sources of interest in the case of source apportionment would require re-running the CTM to create a new set of sensitivities. For this reason, these methods generally are not amenable to use by non-experts.

There additionally exist statistical models based on the results of many CTM runs (e.g., the Response Surface Model, US EPA, 2006; models based on neural networks or neuro-fuzzy systems, Carnevale et al., 2009; or the model by Buonocore et al. (2014)); the requirement of many CTM runs renders these models computationally expensive to create and update.

## A.2 Gaussian

Gaussian plume models (e.g., AERMOD, Cimorelli et al., 2005) and models that are derived from them (e.g., COBRA, US EPA, 2012; APEEP, Muller and Mendelsohn, 2006; SIM-air, Guttikunda, 2009; or the model developed for the US EPA National Air Toxics Assessment (NATA), Logue et al., 2011) analytically estimate the downwind impact of individual sources or source groups. These models are computationally inexpensive and useful for predicting near-source impacts but are not recommended for predictions of pollution transport over long distances (> 50 km, US EPA, 2015). Additionally, Gaussian plume models generally cannot robustly represent nonlinear or spatially variable rates of formation and evaporation of secondary PM<sub>2.5</sub> (Seinfeld and Pandis, 2006).

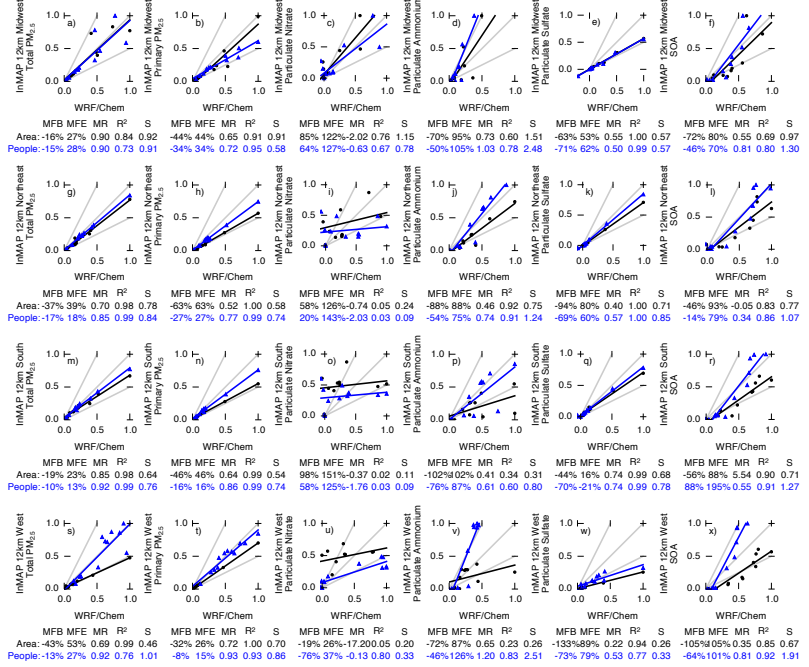


Figure 5: Region-specific comparisons of area-weighted (black dots) and population-weighted (blue triangles) annual average predictions of total PM<sub>2.5</sub> and its subspecies between WRF-Chem ( $x$  axis) and InMAP ( $y$  axis) for 11 emissions scenarios. To assist in comparison between area- and population-weighted predictions, concentrations shown here are normalized so that the largest value in each comparison equals one. The gray lines represent InMAP : WRF-Chem ratios of 1 : 1, 2 : 1, and 1 : 2. The black and blue lines represent least-squares regressions. Performance statistics for each comparison are listed below the plots. Abbreviations: MFB = mean fractional bias; MFE = mean fractional error; MR = model ratio;  $R^2$  = squared Pearson correlation coefficient;  $S$  = slope of regression line.

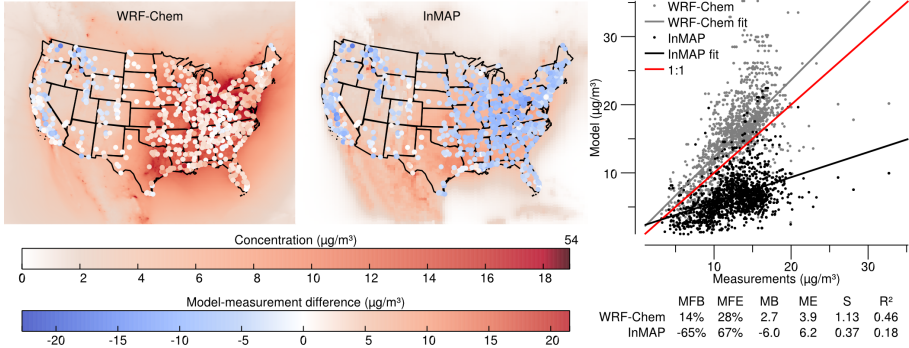


Figure 6: Comparison of WRF-Chem and InMAP performance in predicting annual average observed total PM<sub>2.5</sub> concentrations. The background colors in the maps represent predicted concentrations, and the colors of the circles on the maps represent the difference between modeled and measured values at measurement locations. For the comparison shown here, on average WRF-Chem overpredicts and InMAP underpredicts as compared to observations. Abbreviations: MFB = mean fractional bias; MFE = mean fractional error; MB = mean bias; ME = mean error; MR = model ratio;  $S$  = slope of regression line;  $R^2$  = squared Pearson correlation coefficient.

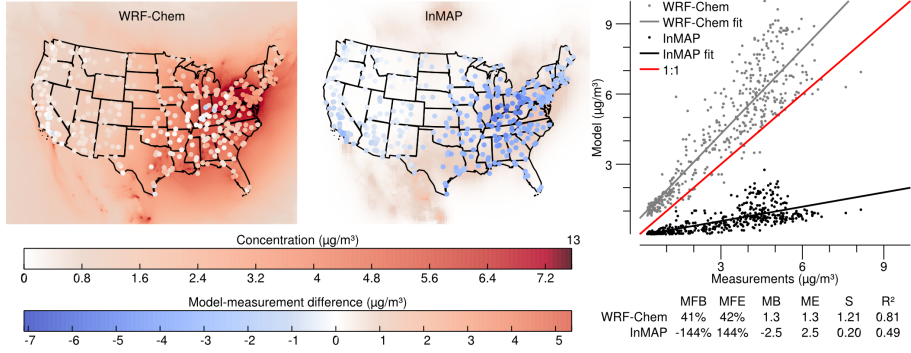


Figure 7: Comparison of WRF-Chem and InMAP performance in predicting annual average observed particulate  $\text{SO}_4$  concentrations. The background colors in the maps represent predicted concentrations, and the colors of the circles on the maps represent the difference between modeled and measured values at measurement locations. Abbreviations: MFB = mean fractional bias; MFE = mean fractional error; MB = mean bias; ME = mean error; MR = model ratio; S = slope of regression line;  $R^2$  = squared Pearson correlation coefficient.

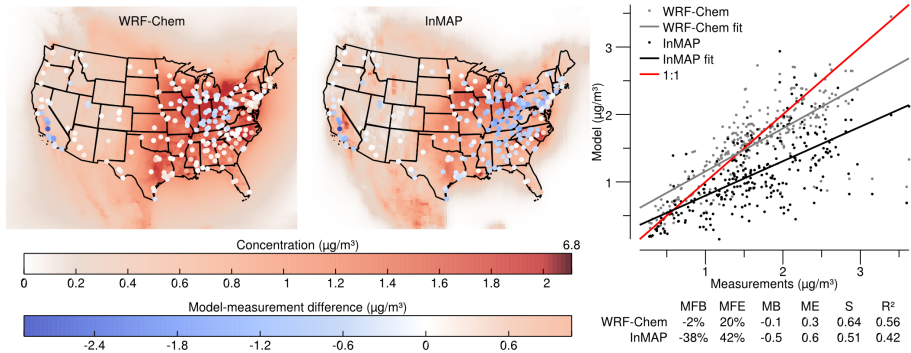


Figure 8: Comparison of WRF-Chem and InMAP performance in predicting annual average observed particulate  $\text{NH}_4$  concentrations. The background colors in the maps represent modeled concentrations, and the colors of the circles on the maps represent the difference between modeled and measured values at measurement locations. Abbreviations: MFB = mean fractional bias; MFE = mean fractional error; MB = mean bias; ME = mean error; MR = model ratio; S = slope of regression line;  $R^2$  = squared Pearson correlation coefficient.

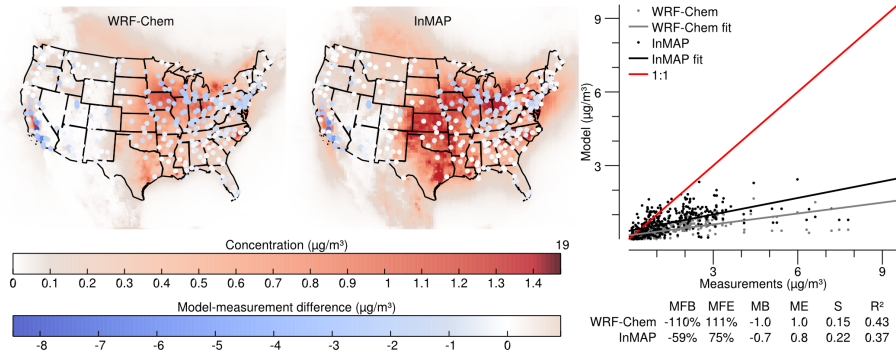


Figure 9: Comparison of WRF-Chem and InMAP performance in predicting annual average observed particulate  $\text{NO}_3$  concentrations. The background colors in the maps represent modeled concentrations, and the colors of the circles on the maps represent the difference between modeled and measured values at measurement locations. Abbreviations: MFB = mean fractional bias; MFE = mean fractional error; MB = mean bias; ME = mean error; MR = model ratio; S = slope of regression line;  $R^2$  = squared Pearson correlation coefficient.

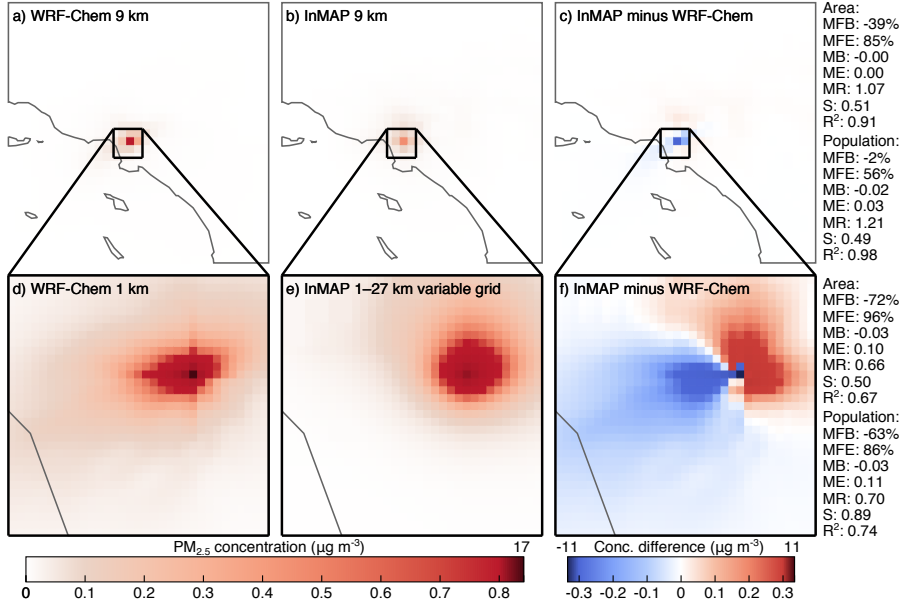


Figure 10: Comparison of WRF-Chem and InMAP performance in predicting the impacts of 100 tons per year of primary nonreactive PM<sub>2.5</sub> emissions at 9 km (panels a and b), 1 km (panel d), and 1–27 km variable (panel f) grid resolutions. InMAP predictions in panel e are based on meteorology from the 9 km-resolution WRF-Chem simulation (panel a) rather than the 1 km-resolution simulation (panel d). Panels c and f show the differences between the panels to their left. Area- and population-weighted statistics are shown on the right. Abbreviations: MFB = mean fractional bias; MFE = mean fractional error; MB = mean bias; ME = mean error; MR = model ratio; S = slope of regression line;  $R^2$  = squared Pearson correlation coefficient.

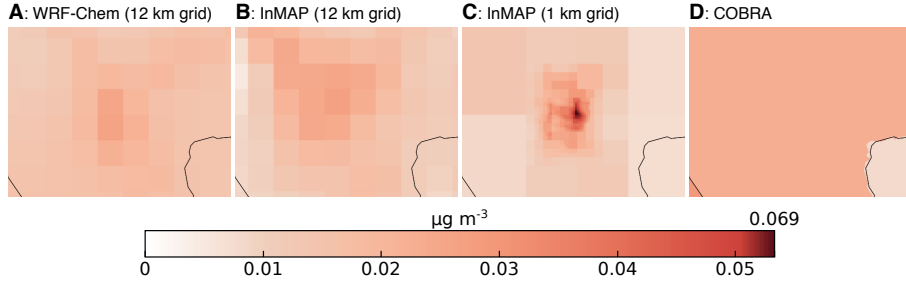


Figure 11: A detail view of Fig. 2 centered on the city of Las Vegas. Changes in concentrations resulting from one of the emissions scenarios as calculated by (a) WRF-Chem, (b) InMAP with a 12 km resolution grid, (c) InMAP with a 1 to 48 km variable resolution grid, and (d) COBRA, which has county-level outputs. InMAP 1 km (panel c) provides the highest spatial resolution, which is important for calculating health impacts in areas with high spatial gradients in pollutant concentration and in population.

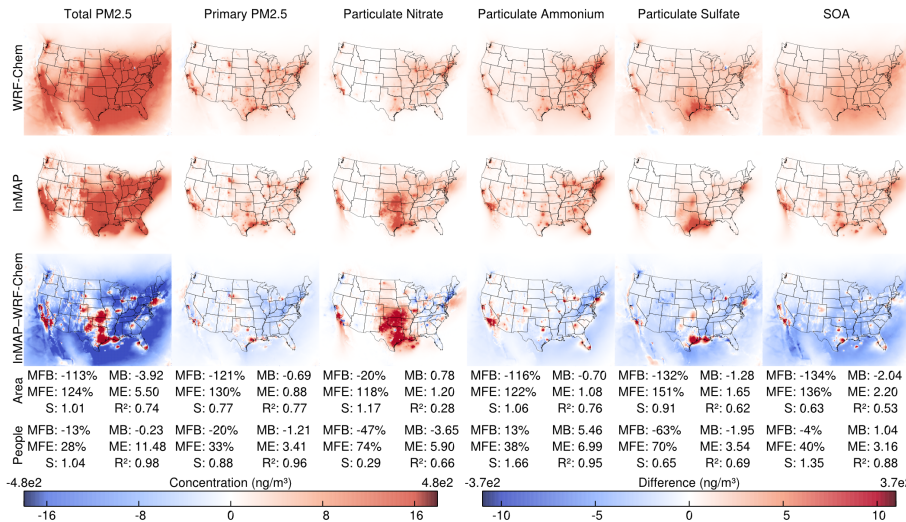


Figure 12: Annual average increases in pollutant concentrations caused by an emission scenario with **on-road emissions from gasoline powered vehicles** as the largest emissions source, as predicted by WRF-Chem (first row) and InMAP with a 12 km resolution grid (second row), as well as the difference between the two models (third row). Colors in the first two rows correspond to the legend on the left and colors in the third row correspond to the legend on the right. For ease of viewing, there is a discontinuity at the 99th percentile of concentration values in each color scale. Abbreviations: MFB = mean fractional bias; MFE = mean fractional error; MB = mean bias; ME = mean error; S = slope of regression line;  $R^2$  = squared Pearson correlation coefficient.

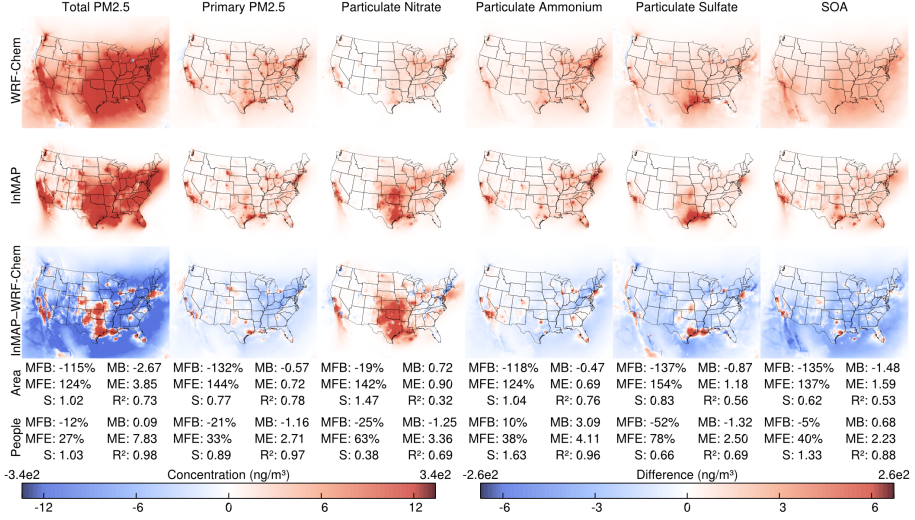


Figure 13: Annual average increases in pollutant concentrations caused by an emission scenario with **on-road emissions from hybrid gasoline-electric powered vehicles** as the largest emissions source, as predicted by WRF-Chem (first row) and InMAP with a 12 km resolution grid (second row), as well as the difference between the two models (third row). Colors in the first two rows correspond to the legend on the left and colors in the third row correspond to the legend on the right. For ease of viewing, there is a discontinuity at the 99th percentile of concentration values in each color scale. Abbreviations: MFB = mean fractional bias; MFE = mean fractional error; MB = mean bias; ME = mean error; S = slope of regression line;  $R^2$  = squared Pearson correlation coefficient.

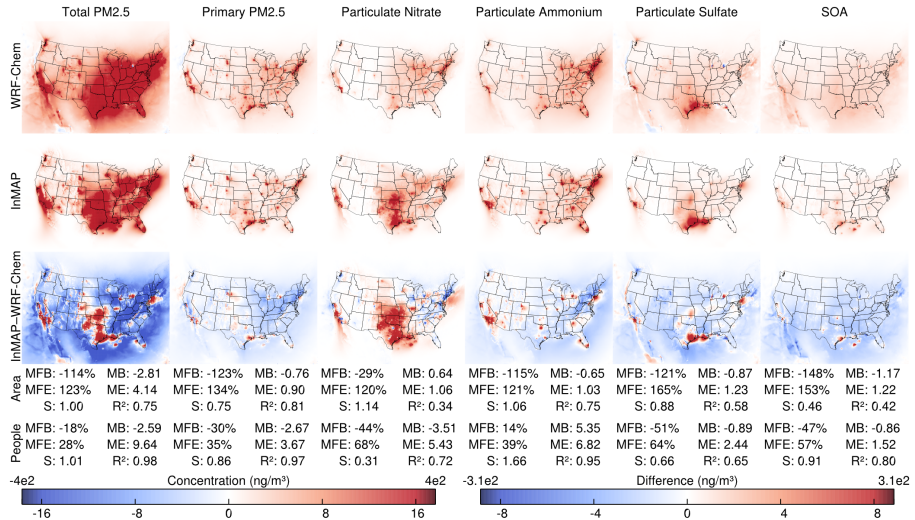


Figure 14: Annual average increases in pollutant concentrations caused by an emission scenario with **on-road emissions from diesel powered vehicles** as the largest emissions source, as predicted by WRF-Chem (first row) and InMAP with a 12 km resolution grid (second row), as well as the difference between the two models (third row). Colors in the first two rows correspond to the legend on the left and colors in the third row correspond to the legend on the right. For ease of viewing, there is a discontinuity at the 99th percentile of concentration values in each color scale. Abbreviations: MFB = mean fractional bias; MFE = mean fractional error; MB = mean bias; ME = mean error; S = slope of regression line;  $R^2$  = squared Pearson correlation coefficient.

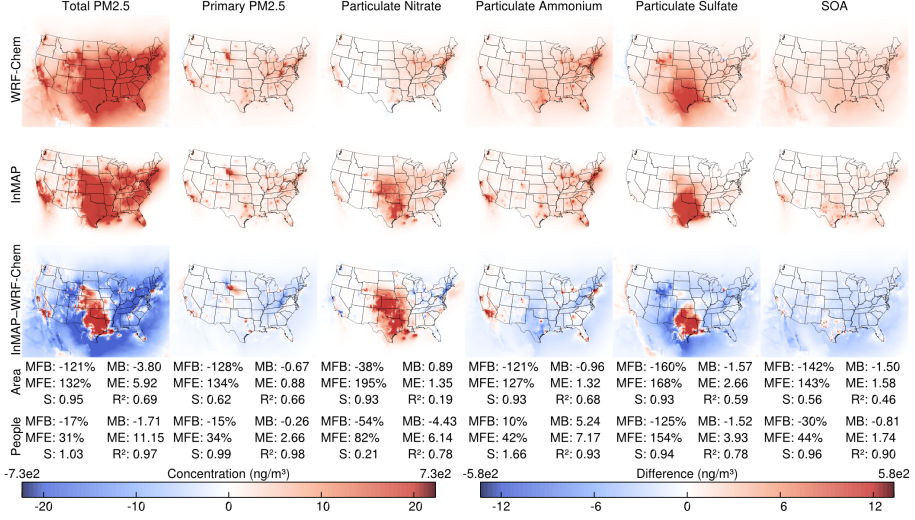


Figure 15: Annual average increases in pollutant concentrations caused by an emission scenario with **on-road emissions from compressed natural gas (CNG) powered vehicles** as the largest emissions source, as predicted by WRF-Chem (first row) and InMAP with a 12 km resolution grid (second row), as well as the difference between the two models (third row). Colors in the first two rows correspond to the legend on the left and colors in the third row correspond to the legend on the right. For ease of viewing, there is a discontinuity at the 99th percentile of concentration values in each color scale. Abbreviations: MFB = mean fractional bias; MFE = mean fractional error; MB = mean bias; ME = mean error; S = slope of regression line;  $R^2$  = squared Pearson correlation coefficient.

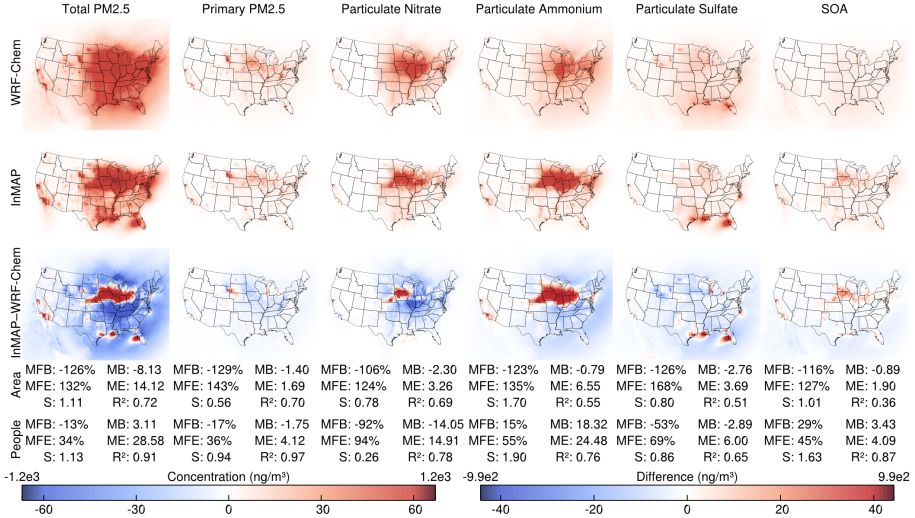


Figure 16: Annual average increases in pollutant concentrations caused by an emission scenario with **industrial emissions, agricultural emissions, and on-road emissions from ethanol powered vehicles** as the largest emissions sources, as predicted by WRF-Chem (first row) and InMAP with a 12 km resolution grid (second row), as well as the difference between the two models (third row). Colors in the first two rows correspond to the legend on the left and colors in the third row correspond to the legend on the right. For ease of viewing, there is a discontinuity at the 99th percentile of concentration values in each color scale. Abbreviations: MFB = mean fractional bias; MFE = mean fractional error; MB = mean bias; ME = mean error; S = slope of regression line;  $R^2$  = squared Pearson correlation coefficient.

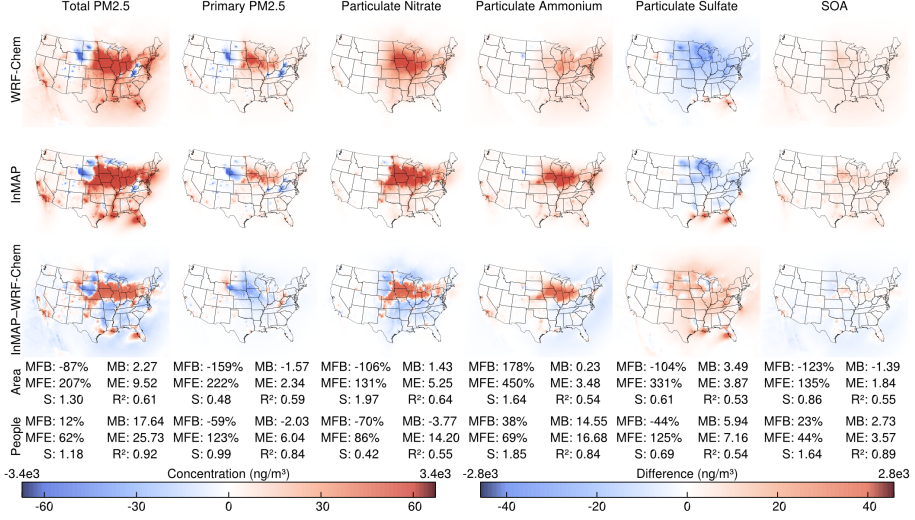


Figure 17: Annual average increases in pollutant concentrations caused by an emission scenario with **industrial emissions, agricultural emissions, and on-road emissions from ethanol powered vehicles** as the largest emissions sources, as predicted by WRF-Chem (first row) and InMAP with a 12 km resolution grid (second row), as well as the difference between the two models (third row). Colors in the first two rows correspond to the legend on the left and colors in the third row correspond to the legend on the right. For ease of viewing, there is a discontinuity at the 99th percentile of concentration values in each color scale. Abbreviations: MFB = mean fractional bias; MFE = mean fractional error; MB = mean bias; ME = mean error; S = slope of regression line;  $R^2$  = squared Pearson correlation coefficient.

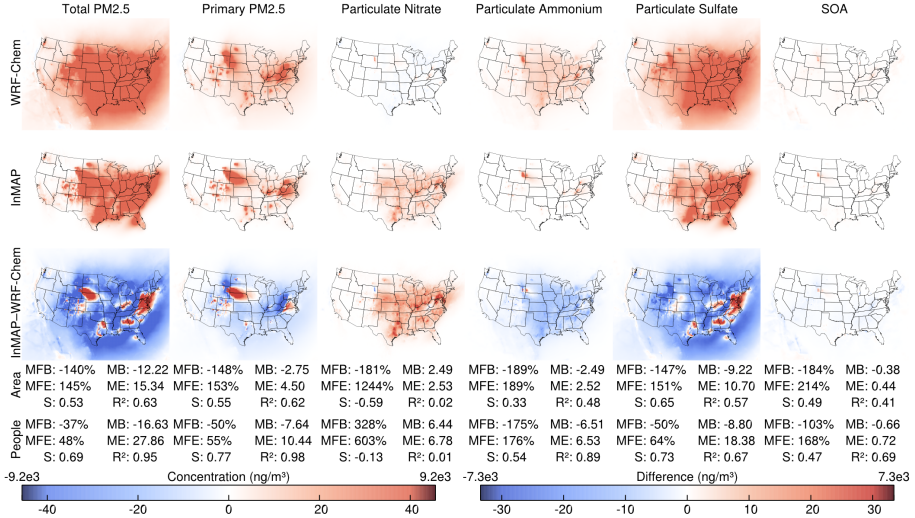


Figure 18: Annual average increases in pollutant concentrations caused by an emission scenario with **emissions from coal- and natural gas-powered electric generation and from coal mining** as the largest emissions sources, as predicted by WRF-Chem (first row) and InMAP with a 12 km resolution grid (second row), as well as the difference between the two models (third row). Colors in the first two rows correspond to the legend on the left and colors in the third row correspond to the legend on the right. For ease of viewing, there is a discontinuity at the 99th percentile of concentration values in each color scale. Abbreviations: MFB = mean fractional bias; MFE = mean fractional error; MB = mean bias; ME = mean error; S = slope of regression line;  $R^2$  = squared Pearson correlation coefficient.

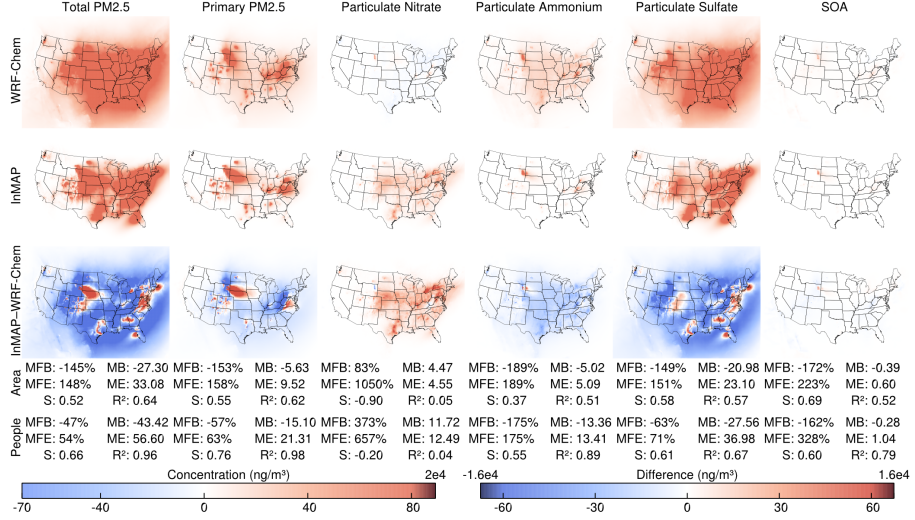


Figure 19: Annual average pollutant concentrations caused by an emission scenario with **emissions from coal-powered electric generation and from coal mining** as the largest emissions sources, as predicted by WRF-Chem (first row) and InMAP with a 12 km resolution grid (second row), as well as the difference between the two models (third row). Colors in the first two rows correspond to the legend on the left and colors in the third row correspond to the legend on the right. For ease of viewing, there is a discontinuity at the 99th percentile of concentration values in each color scale. Abbreviations: MFB = mean fractional bias; MFE = mean fractional error; MB = mean bias; ME = mean error; S = slope of regression line;  $R^2$  = squared Pearson correlation coefficient.

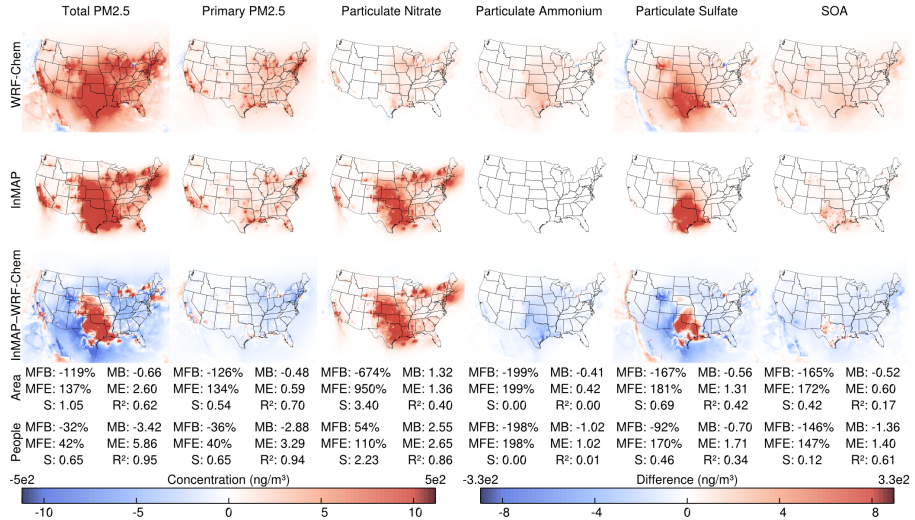


Figure 20: Annual average pollutant concentrations caused by an emission scenario with **emissions from natural-gas powered electric generation and natural gas extraction and processing** as the largest emissions sources, as predicted by WRF-Chem (first row) and InMAP with a 12 km resolution grid (second row), as well as the difference between the two models (third row). Colors in the first two rows correspond to the legend on the left and colors in the third row correspond to the legend on the right. For ease of viewing, there is a discontinuity at the 99th percentile of concentration values in each color scale. Abbreviations: MFB = mean fractional bias; MFE = mean fractional error; MB = mean bias; ME = mean error; S = slope of regression line;  $R^2$  = squared Pearson correlation coefficient.

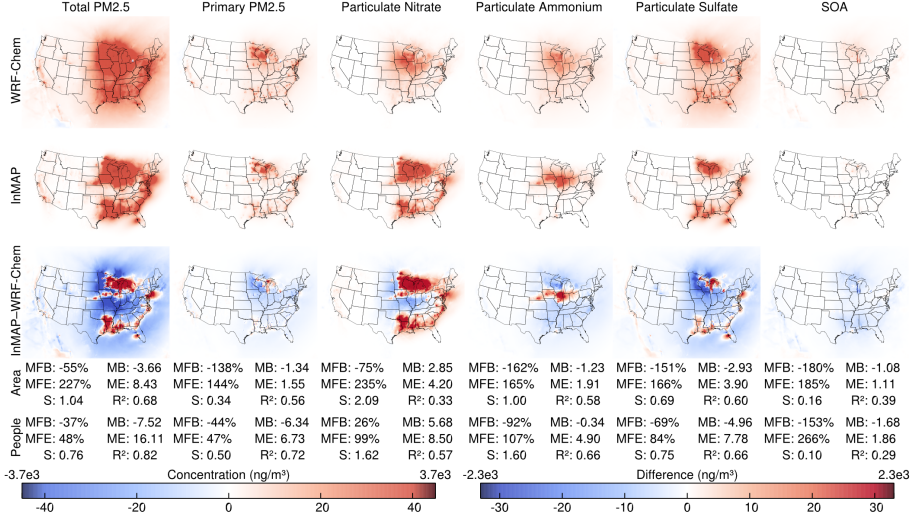


Figure 21: Annual average pollutant concentrations caused by an emission scenario with **emissions from agricultural sources and from biomass-powered electric generation** as the largest emissions sources, as predicted by WRF-Chem (first row) and InMAP with a 12 km resolution grid (second row), as well as the difference between the two models (third row). Colors in the first two rows correspond to the legend on the left and colors in the third row correspond to the legend on the right. For ease of viewing, there is a discontinuity at the 99th percentile of concentration values in each color scale. Abbreviations: MFB = mean fractional bias; MFE = mean fractional error; MB = mean bias; ME = mean error; S = slope of regression line;  $R^2$  = squared Pearson correlation coefficient.

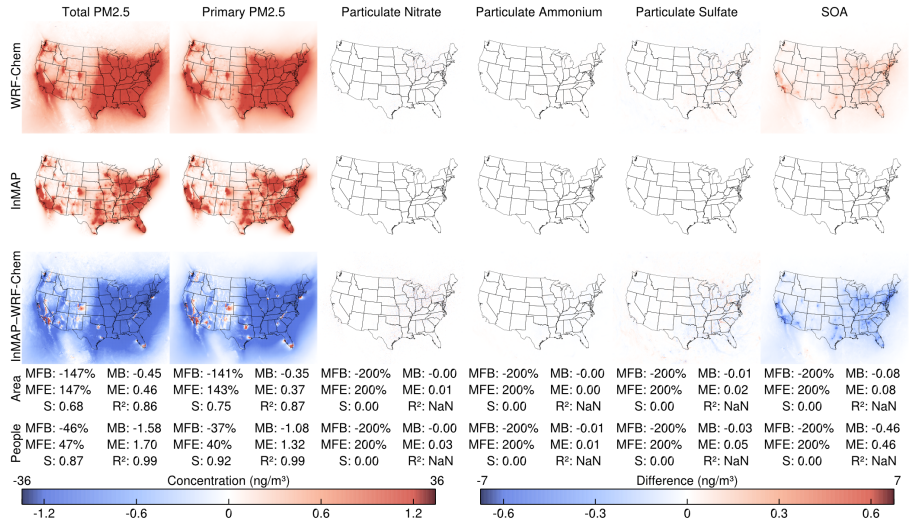


Figure 22: Annual average pollutant concentrations caused by an emission scenario with **on-road emissions from vehicle brake and tire wear** as the only emissions source, as predicted by WRF-Chem (first row) and InMAP with a 12 km resolution grid (second row), as well as the difference between the two models (third row). Colors in the first two rows correspond to the legend on the left and colors in the third row correspond to the legend on the right. For ease of viewing, there is a discontinuity at the 99th percentile of concentration values in each color scale. Abbreviations: MFB = mean fractional bias; MFE = mean fractional error; MB = mean bias; ME = mean error; S = slope of regression line;  $R^2$  = squared Pearson correlation coefficient.

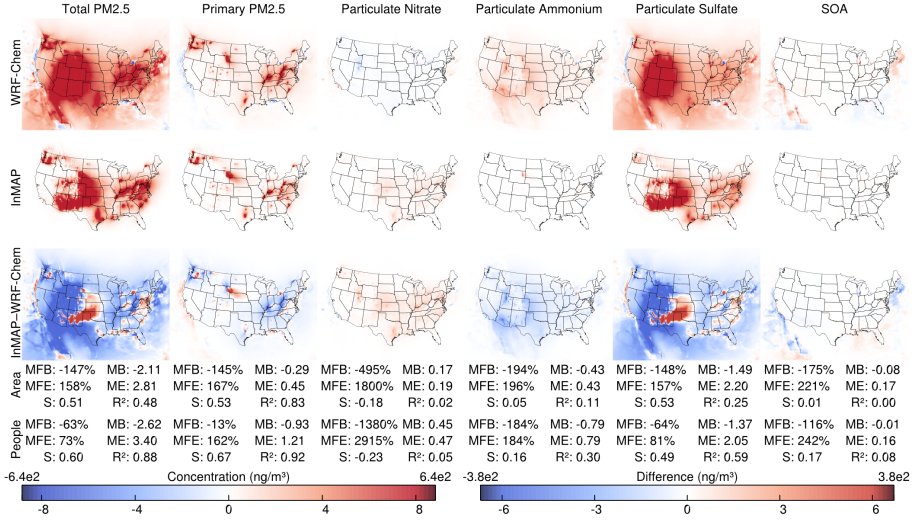


Figure 23: Annual average pollutant concentrations caused by an emission scenario with **emissions from mineral extraction and electricity production** as the largest emissions sources, as predicted by WRF-Chem (first row) and InMAP with a 12 km resolution grid (second row), as well as the difference between the two models (third row). Colors in the first two rows correspond to the legend on the left and colors in the third row correspond to the legend on the right. For ease of viewing, there is a discontinuity at the 99th percentile of concentration values in each color scale. Abbreviations: MFB = mean fractional bias; MFE = mean fractional error; MB = mean bias; ME = mean error; S = slope of regression line;  $R^2$  = squared Pearson correlation coefficient.

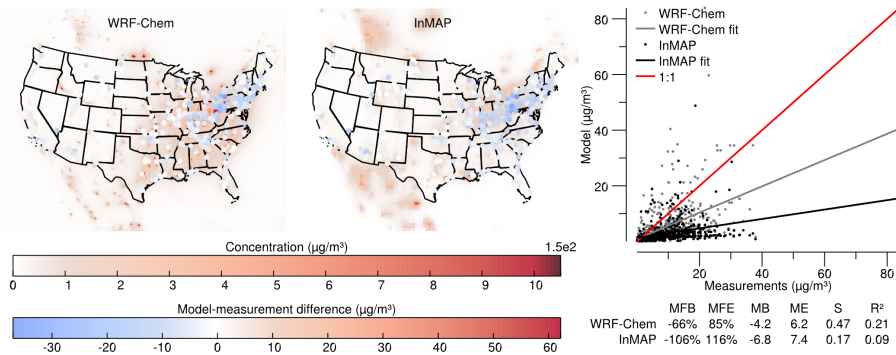


Figure 24: Comparison of WRF-Chem and InMAP performance in predicting annual average observed  $\text{SO}_x$  concentrations. The background colors in the maps represent predicted concentrations, and the colors of the circles on the maps represent the difference between modeled and measured values at measurement locations. Abbreviations: MFB = mean fractional bias; MFE = mean fractional error; MB = mean bias; ME = mean error; MR = model ratio; S = slope of regression line;  $R^2$  = squared Pearson correlation coefficient.

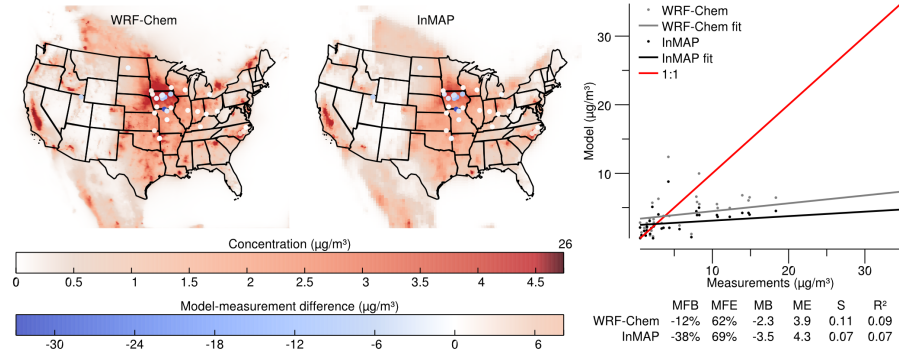


Figure 25: Comparison of WRF-Chem and InMAP performance in predicting annual average observed  $\text{NH}_3$  concentrations. The background colors in the maps represent modeled concentrations, and the colors of the circles on the maps represent the difference between modeled and measured values at measurement locations. Abbreviations: MFB = mean fractional bias; MFE = mean fractional error; MB = mean bias; ME = mean error; MR = model ratio; S = slope of regression line;  $R^2$  = squared Pearson correlation coefficient.

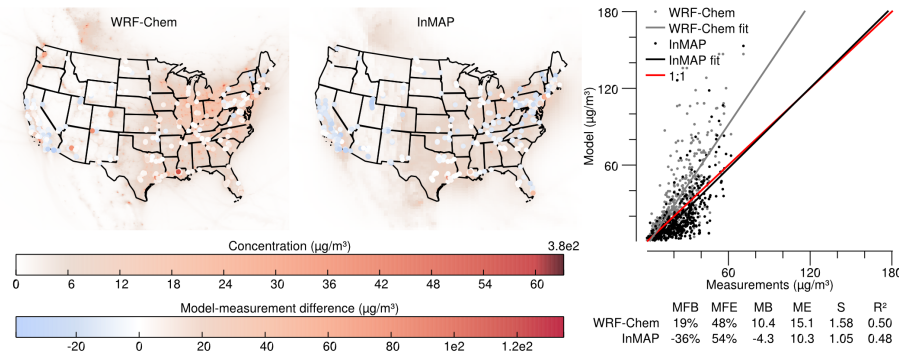


Figure 26: Comparison of WRF-Chem and InMAP performance in predicting annual average observed  $\text{NO}_x$  concentrations. The background colors in the maps represent modeled concentrations, and the colors of the circles on the maps represent the difference between modeled and measured values at measurement locations. Abbreviations: MFB = mean fractional bias; MFE = mean fractional error; MB = mean bias; ME = mean error; MR = model ratio; S = slope of regression line;  $R^2$  = squared Pearson correlation coefficient.



Figure 27: Boundaries of US regions used in this article.

Table 1: Names of WRF-Chem Variables used by the InMAP Preprocessor and their Descriptions

Name(s)	Description and use in InMAP preprocessor
hc5, hc8, olt, oli, tol, xyl, csl, cvasoa1, cvasoa2, cvasoa3, cvasoa4	Anthropogenic VOCs that are SOA precursors; used to determine VOA/SOA partitioning
asoal1, asoa1j, asoa2i, asoa2j, asoa3i, asoa3j, asoa4i, asoa4j	Anthropogenic SOA; used to determine VOA/SOA partitioning
iso, api, sesq, lim, cvbsoa1, cvbsoa2, cvbsoa3, cvbsoa4	Biogenic VOCs that are SOA precursors; used for model evaluation
bsoa1i, bsoa1j, bsoa2i, bsoa2j, bsoa3i, bsoa3j, bsoa4i, bsoa4j	Biogenic SOA; used for model evaluation
no, no2	Components of $\text{NO}_x$ ; used to determine $\text{NO}_x/p\text{NO}_3$ partitioning
no3ai, no3aj	Components of $p\text{NO}_3$ ; used to determine $\text{NO}_x/p\text{NO}_3$ partitioning
so2, sulf	Gaseous $\text{SO}_2$ and sulfate; used to determine $\text{SO}_x/p\text{SO}_4$ partitioning
so4ai, so4aj	Particulate $\text{SO}_4$ ; used to determine $\text{SO}_x/p\text{SO}_4$ partitioning
nh3	Ammonia; used to determine $\text{NH}_3/p\text{NH}_4$ partitioning
nh4ai, nh4aj	Particulate Ammonium; used to determine $\text{NH}_3/p\text{NH}_4$ partitioning
PM2.5_DRY	Total PM <sub>2.5</sub> concentration in the baseline simulation; used for model evaluation
U, V, W	Wind fields; used to determine advection and mixing coefficients
PBLH	Planetary boundary layer height; used to determine mixing coefficients
PHB, PH	Base state geopotential and perturbation geopotential; used to calculate layer heights
HFX	Surface heat flux; used to determine mixing and dry deposition
UST	Friction velocity; used to determine mixing and dry deposition
T	Temperature; used to calculate chemical reaction rates and plume rise
PB, P	Base state pressure plus perturbation pressure; used to calculate chemical reaction rates and plume rise
ho, h2o2	Hydroxyl radical and hydrogen peroxide concentrations; used to calculate chemical reaction rates
LU_INDEX	Land use type; used to calculate mixing
QRAIN	Mixing ratio of rain; used to calculate wet deposition
CLDFRA	Fraction of grid cell covered by clouds; used to calculate wet deposition
QCLOUD	Cloud mixing ratio; used to calculate aqueous-phase chemical reaction rates
ALT	Inverse air density; used to calculate mixing and to convert between mixing ratio and mass concentration
SWDOWN, GLW	Downward shortwave and longwave radiative flux at ground level; used to calculate dry deposition

### A.3 Lagrangian

Lagrangian models such as CALPUFF (Scire et al., 2000) and HYSPLIT (Draxler and Hess, 1997) track long range transport from individual sources by tracking a packet of air as it interacts with its surroundings. These models typically are less computationally intensive than CTMs if the number of sources is small, but simulating many individual sources over a broad area can be computationally prohibitive.

### A.4 Chemical mass balance

Chemical mass balance models (e.g., CMB: US EPA, 2014) estimate the contribution of different emissions source types to ambient pollution concentrations by analyzing the relative contributions of different chemical tracers and matching them to tracer profiles of known sources. This method is useful for estimating the contribution specific source types, but requires detailed location-specific measurements and can only track contributions from sources with known tracer profiles. Additionally, chemical mass balance models cannot directly predict how changes in emissions would impact concentrations.

## B WRF variables used to create InMAP inputs

## C Spatial discretization algorithm

To use numerical integration to solve the chemical and physical equations that describe the processes relevant to air pollution, a model must break up the spatial and temporal domains of interest into finite elements.

InMAP spatially discretizes the model domain using a variable resolution rectangular grid, where individual grid cells can nest and telescope between lower and higher resolution based on human population density or other attributes. Grid cell resolution is determined by the following algorithm. Given a list of possible grid cell sizes, the model domain is first filled with the lowest resolution grid cells (48 km). Then, the program iterates through the grid cells, determining if the population in each grid cell is above a certain threshold level. If the population in the grid cell is above the threshold level, the grid cell is split into grid cells of the next smallest size. The algorithm recurses through this process until either all of the cells are below the population threshold or the smallest specified grid cell size has been reached. The algorithm also has a second constraint, where any of the smallest-size grid cells having a maximum population density greater than a certain threshold level are kept at the finest resolution. This constraint is important where high population density areas are directly adjacent to low population density areas, such as in coastal cities. Because variability in pollutant concentrations decreases with increased height above the ground, all grid cells above a given height cutoff are kept at the lowest model resolution. As shown in Fig. 1, we use here a spatial domain which covers the contiguous US, southern Canada, and northern Mexico, with grid cell edge lengths of 48, 24, 12, 4, 2, and 1 km, a population threshold of 40 000 people per grid cell, a population density threshold of 5500 people  $\text{km}^{-1}$ , and a height cutoff of the eighth model layer (approximately 1500 m, chosen because this height is usually above the planetary boundary layer). These settings are chosen to achieve a balance between the spatial detail and model runtime. Other spatial domains are possible: the spatial extent of the modeling domain is only limited by the availability of meteorological and chemical input data. Meteorological and chemical properties in InMAP cells that do not exactly coincide with grid cells in the input data set are taken as the average of all input grid cells that they overlap with.

## References

- Ahmadov, R., McKeen, S. A., Robinson, A. L., Bahreini, R., Middlebrook, A. M., de Gouw, J. A., Meagher, J., Hsie, E.-Y., Edgerton, E., Shaw, S., and Trainer, M.: A volatility basis set model for summertime secondary organic aerosols over the eastern United States in 2006, *J. Geophys. Res.*, 117, D06301, doi:10.1029/2011JD016831, 2012.
- American Society of Mechanical Engineers (ASME): Recommended Guide for the Prediction of the Dispersion of Airborne Effluents, ASME, New York, NY, 2nd edn., 1973.
- Boylan, J. W. and Russell, A. G.: PM and light extinction model performance metrics, goals, and criteria for three-dimensional air quality models, *Atmos. Environ.*, 40, 4946–4959, doi:10.1016/j.atmosenv.2005.09.087, 2006.
- Brook, R. D., Rajagopalan, S., Pope III, C. A., Brook, J. R., Bhatnagar, A., Diez-Roux, A. V., Holguin, F., Hong, Y., Luepker, R. V., Mittleman, M. A., Peters, A., Siscovick, D., Smith, S. C. J., Whitsel, L., and Kaufman, J. D.: Particulate matter air pollution and cardiovascular disease: an update to the scientific statement from the american heart association, *Circulation*, 121, 2331–2378, doi:10.1161/CIR.0b013e3181dbece1, 2010.
- Buonocore, J. J., Dong, X., Spengler, J. D., Fu, J. S., and Levy, J. I.: Using the Community Multiscale Air Quality (CMAQ) model to estimate public health impacts of PM2.5 from individual power plants, *Environ. Int.*, 68, 200–208, doi:10.1016/j.envint.2014.03.031, 2014.
- Byun, D. W. and Ching, J. K. S.: Science Algorithms of the EPA Models-3 Community Multiscale Air Quality (CMAQ) Modeling System, Tech. rep., US Environmental Protection Agency #EPA/600/R-99/030, Washington, D.C., available at: <http://nepis.epa.gov/EPA/html/DLwait.htm?url=/Exe/ZyPDF.cgi/30003R9Y.PDF?Dockey=30003R9Y.PDF> (last access: 26 October 2015), 1999.
- Carnevale, C., Finzi, G., Pisoni, E., and Volta, M.: Neuro-fuzzy and neural network systems for air quality control, *Atmos. Env.*, 43, 4811–4821, doi:, 2009.

- Cimorelli, A. J., Perry, S. G., Venkatram, A., Weil, J. C., Paine, R. J., Wilson, R. B., Lee, R. F., Peters, W. D., and Brode, R. W.: AERMOD: a dispersion model for industrial source applications. Part I: General model formulation and boundary layer characterization, *J. Appl. Meteorol.*, 44, 682–693, doi:10.1175/JAM2227.1, 2005.
- Cohon, J. L., Cropper, M. L., Cullen, M. R., Drake, E. M., English, M., Field, C. B., Greenbaum, D. S., Hammitt, J. K., Henderson, R. F., Kling, C. L., Krupnick, A. J., Lee, R., Matthews, H. S., McKone, T. E., Metcalf, G. E., Newell, R. G., Revesz, R. L., Wing, I. S., and Surles, T. G.: Hidden Costs of Energy: Unpriced Consequences of Energy Production and Use, Tech. rep., National Research Council, available at: [http://www.nap.edu/catalog.php?record\\_id=12794](http://www.nap.edu/catalog.php?record_id=12794) (last access: 26 October 2015), 2009.
- Courant, R., Friedrichs, K., and Lewy, H.: Über die partiellen Differenzengleichungen der mathematischen Physik, *Math. Ann.*, 100, 32–74, doi:10.1007/BF01448839, 1928.
- Dedoussi, I. C. and Barrett, S. R. H.: Air pollution and early deaths in the United States. Part II: Attribution of PM<sub>2.5</sub> exposure to emissions species, time, location and sector, *Atmos. Environ.*, 99, 610–617, doi:10.1016/j.atmosenv.2014.10.033, 2014.
- Delucchi, M. A.: Environmental externalities of motor-vehicle use in the US, *J. Transp. Econ. Policy*, 34, 135–168, 2000.
- Draxler, R. R. and Hess, G. D.: Description of the HYSPLIT\_4 Modeling System, Tech. rep., NOAA Technical Memo. #ERL ARL-224, Silver Spring, MD, available at: <http://www.ciecm.uhu.es/hysplitweb08/document/ar1-224.pdf> (last access: 26 October 2015), 1997.
- ENVIRON: User's Guide – Comprehensive Air-Quality Model with Extensions, Tech. rep., ENVIRON International Corporation, Novato, CA, available at: [http://www.camx.com/files/camxusersguide\\_v5-40.aspx](http://www.camx.com/files/camxusersguide_v5-40.aspx) (last access: 26 October 2015), 2011.
- Fountoukis, C., Koraj, D., Denier van der Gon, H. A. C., Charalampidis, P. E., Pilinis, C., and Pandis, S. N.: Impact of grid resolution on the predicted fine PM by a regional 3-D chemical transport model, *Atmos. Environ.*, 68, 24–32, doi:10.1016/j.atmosenv.2012.11.008, 2013.
- Grell, G. A., Peckham, S. E., Schmitz, R., McKeen, S. A., Frost, G., Skamarock, W. C., and Eder, B.: Fully coupled “online” chemistry within the WRF model, *Atmos. Environ.*, 39, 6957–6975, doi:10.1016/j.atmosenv.2005.04.027, 2005.
- Guttikunda, S. K.: SIM-air modeling tools, available at: <http://urbanemissions.info/model-tools.html> (last access: 26 October 2015), 2009.
- Hakami, A., Henze, D. K., Seinfeld, J. H., Singh, K., Sandu, A., Kim, S., Byun, D., and Li, Q.: The Adjoint of CMAQ, *Environ. Sci. Technol.*, 41, 7807–7817, 2007.
- Jacobson, M. Z.: GATOR-GCMM: a global-through urban-scale air pollution and weather forecast model: 1. Model design and treatment of subgrid soil, vegetation, roads, rooftops, water, sea ice, and snow, *J. Geophys. Res.*, 106, 5385–5401, doi:10.1029/2000JD900560, 2001.
- Künzli, N., Medina, S., Kaiser, R., Quénel, P., Horak, F. J., and Studnicka, M.: Assessment of deaths attributable to air pollution: should we use risk estimates based on time series or on cohort studies?, *Am. J. Epidemiol.*, 153, 1050–1055, 2001.
- Lelieveld, J., Evans, J. S., Fnais, M., Giannadaki, D., and Pozzer, A.: The contribution of outdoor air pollution sources to premature mortality on a global scale, *Nature*, 525, 367–371, doi:10.1038/nature15371, 2015.

Li, Y., Henze, D. K., Jack, D., and Kinney, P. L.: The influence of air quality model resolution on health impact assessment for fine particulate matter and its components, *Air Qual. Atmos. Heal.*, 1–18, doi:10.1007/s11869-015-0321-z, 2015.

Liang, M.: Reduced-Complexity Models (RCMs) for River Delta Formation with Channel Dynamics, PhD, University of Minnesota, available at: <http://purl.umn.edu/155962> (last access: 26 October 2015), 2013.

Liang, M., Voller, V. R., and Paola, C.: A reduced-complexity model for river delta formation – Part 1: Modeling deltas with channel dynamics, *Earth Surf. Dyn.*, 3, 67–86, doi:10.5194/esurf-3-67-2015, 2015.

Lim, S. S., Vos, T., Flaxman, A. D., et al.: A comparative risk assessment of burden of disease and injury attributable to 67 risk factors and risk factor clusters in 21 regions, 1990–2010: a systematic analysis for the Global Burden of Disease Study 2010, *Lancet*, 380, 2224–2260, doi:10.1016/S0140-6736(12)61766-8, 2012.

Logue, J. M., Small, M. J., and Robinson, A. L.: Evaluating the national air toxics assessment (NATA): comparison of predicted and measured air toxics concentrations, risks, and sources in Pittsburgh, Pennsylvania, *Atmos. Environ.*, 45, 476–484, doi:10.1016/j.atmosenv.2010.09.053, 2011.

Muller, N. Z. and Mendelsohn, R.: The Air Pollution Emission Experiments and Policy Analysis Model (APEEP): Technical Appendix, Tech. rep., available at: <https://sites.google.com/site/nickmullershhomepage/home/ap2-apeep-model-2> (last access: 26 October 2015), 2006.

Pleim, J. E.: A combined local and nonlocal closure model for the atmospheric boundary layer. Part I: Model description and testing, *J. Appl. Meteorol. Clim.*, 46, 1383–1395, doi:10.1175/JAM2539.1, 2007.

Pope III, C. A. and Dockery, D. W.: Health effects of fine particulate air pollution: lines that connect, *J. Air Waste Manage.*, 56, 709 –742, 2006.

Scire, J. S., Strimaitis, D. G., and Yamartino, R. J.: A User's Guide for the CALPUFF Dispersion Model, Tech. Rep. January, Earth Tech, Inc., Concord, MA, available at: [http://www.src.com/calpuff/download/CALPUFF\\_UsersGuide.pdf](http://www.src.com/calpuff/download/CALPUFF_UsersGuide.pdf) (last access: 26 October 2015), 2000.

Seinfeld, J. H. and Pandis, S. N.: Atmospheric Chemistry and Physics: From Air Pollution to Climate Change, Wiley, Hoboken, N. J., 2nd edn., 2006.

Simpson, D., Fagerli, H., Jonson, J. E., Tsyró, S., Wind, P., and Tuovinen, J.-P.: Transboundary Acidification, Eutrophication and Ground Level Ozone in Europe, Part I: Unified EMEP Model Description, Tech. rep., Norwegian Meteorological Institute, available at: [http://www.emep.int/publ/reports/2003/emepr\\_report\\_1\\_part1\\_2003.pdf](http://www.emep.int/publ/reports/2003/emepr_report_1_part1_2003.pdf) (last access: 26 October 2015), 2003.

Tessum, C. W., Marshall, J. D., and Hill, J. D.: A spatially and temporally explicit life cycle inventory of air pollutants from gasoline and ethanol in the United States, *Environ. Sci. Technol.*, 46, 11408–11417, doi:10.1021/es3010514, 2012.

Tessum, C. W., Hill, J. D., and Marshall, J. D.: Life cycle air quality impacts of conventional and alternative light-duty transportation in the United States, *P. Natl. Acad. Sci. USA*, 111, 18490–18495, 2014.

Tessum, C. W., Hill, J. D., and Marshall, J. D.: Twelve-month, 12 km resolution North American WRF-Chem v3.4 air quality simulation: performance evaluation, *Geosci. Model Dev.*, 8, 957–973, doi:10.5194/gmd-8-957-2015, 2015.

Thunis, P., Pederzoli, A., and Pernigotti, D.: Performance criteria to evaluate air quality modeling applications, *Atmos. Env.*, 59, 476–482, doi:, 2012.

US EPA: AirData, available at: [http://aqsdr1.epa.gov/aqsweb/aqstmp/airdata/download\\_files.html](http://aqsdr1.epa.gov/aqsweb/aqstmp/airdata/download_files.html) (last access: 26 October 2015), 2005.

US EPA: Technical Support Document for the Proposed PM NAAQS Rule: Response Surface Modeling, Tech. Rep. February, US Environmental Protection Agency, Research Triangle Park, NC, available at: [http://www.epa.gov/scram001/reports/pmnnaqs\\_tsd\\_rsm\\_all\\_021606.pdf](http://www.epa.gov/scram001/reports/pmnnaqs_tsd_rsm_all_021606.pdf) (last access: 26 October 2015), 2006.

US EPA: User's Manual for the Co-Benefits Risk Assessment (COBRA) Screening Model, Tech. rep., US Environmental Protection Agency, Washington, D.C., available at: <http://epa.gov/statelocalclimate/documents/pdf/cobra-2.61-user-manual-july-2013.pdf> (last access: 26 October 2015), 2012.

EPA-CMB8.2 Users Manual, Tech. rep., US Environmental Protection Agency #EPA-452/R-04-011, available at: <http://www3.epa.gov/ttn/scram/models/receptor/EPA-CMB82Manual.pdf> (last access: 27 January 2016), 2004.

US EPA: Revision to the Guideline on Air Quality Models: Enhancements to the AERMOD Dispersion Modeling System and Incorporation of Approaches to Address Ozone and Fine Particulate Matter, Tech. rep., US Environmental Protection Agency #2060-AS54, available at: [http://www.epa.gov/ttn/scram/11thmodconf/9930-11-OAR\\_AppendixW\\_Proposal.pdf](http://www.epa.gov/ttn/scram/11thmodconf/9930-11-OAR_AppendixW_Proposal.pdf) (last access: 26 October 2015), 2015.

Wagstrom, K. M., Pandis, S. N., Yarwood, G., Wilson, G. M., and Morris, R. E.: Development and application of a computationally efficient particulate matter apportionment algorithm in a three-dimensional chemical transport model, *Atmos. Environ.*, 42, 5650–5659, doi:10.1016/j.atmosenv.2008.03.012, 2008.

Walmsley, J. L. and Wesely, M. L.: Modification of coded parametrizations of surface resistances to gaseous dry deposition, *Atmos. Environ.*, 30, 1181–1188, doi:10.1016/1352-2310(95)00403-3, 1996.

Wesely, M. L.: Parameterization of surface resistances to gaseous dry deposition in regional-scale numerical models, *Atmos. Environ.*, 23, 1293–1304, doi:10.1016/0004-6981(89)90153-4, 1989.

Wilson, R.: Turbulent diffusivity in the free atmosphere inferred from MST radar measurements: a review, *Ann. Geophys.*, 22, 3869–3887, 2004.

Zhang, W., Capps, S. L., Hu, Y., Nenes, A., Napelenok, S. L., and Russell, A. G.: Development of the high-order decoupled direct method in three dimensions for particulate matter: enabling advanced sensitivity analysis in air quality models, *Geosci. Model Dev.*, 5, 355–368, doi:10.5194/gmd-5-355-2012, 2012.